

Probing the Disk–Jet Connection of the Radio Galaxy 3C 120 Observed with Suzaku

Jun KATAOKA,¹ James N. REEVES,² Kazushi IWASAWA,³ Alex G. MARKOWITZ,² Richard F. MUSHOTZKY,²
Makoto ARIMOTO,¹ Tadayuki TAKAHASHI,⁴ Yoshihiro TSUBUKU,¹ Masayoshi USHIO,⁴ Shin WATANABE,⁴
Luigi C. GALLO,^{3,4} Greg M. MADEJSKI,⁵ Yuichi TERASHIMA,⁶ Naoki ISOBE,⁷ Makoto S. TASHIRO,⁸
and Takayoshi KOHMURA⁹

¹*Department of Physics, Tokyo Institute of Technology, Meguro, Tokyo 152-8551*
kataoka@hp.phys.titech.ac.jp

²*NASA, Goddard Space Flight Center, Greenbelt, MD 20771, USA*

³*Max Planck Institut für extraterrestrische Physik (MPE), Garching, Germany*

⁴*Institute of Space and Astronautical Science, JAXA, Sagamihara, Kanagawa 229-8510*

⁵*Stanford Linear Accelerator Center, Stanford, CA 943099-4349, USA*

⁶*Department of Physics, Ehime University, Matsuyama, Ehime 790-8577*

⁷*Cosmic Radiation Laboratory, Institute of Physical and Chemical Research, Wako, Saitama 351-0198*

⁸*Department of Physics, Saitama University, Sakura, Saitama 338-8570*

⁹*Physics Department, Kogakuin University, Hachioji, Tokyo 192-0015*

(Received 2006 November 27; accepted 2006 December 28)

Abstract

We report on deep (40 ks \times 4) observations of the bright broad line radio galaxy 3C 120 using Suzaku. The observations were spaced one week apart, and sampled a range of continuum fluxes. An excellent broadband spectrum was obtained over two decades of frequency (0.6 to 50 keV) within each 40 ks exposure. We clearly resolved the iron K emission-line complex, finding that it consists of a narrow $K\alpha$ core ($\sigma \simeq 110$ eV or an EW of 60 eV), a 6.9 keV line, and an underlying broad iron line. Our confirmation of the broad line contrasts with the XMM-Newton observation in 2003, where the broad line was not required. The most natural interpretation of the broad line is iron K line emission from a face-on accretion disk that is truncated at $\sim 10 r_g$. Above 10 keV, a relatively weak Compton hump was detected (reflection fraction of $R \simeq 0.6$), superposed on the primary X-ray continuum of $\Gamma \simeq 1.75$. Thanks to the good photon statistics and low background of the Suzaku data, we clearly confirm the spectral evolution of 3C 120, whereby the variability amplitude decreases with increasing energy. More strikingly, we discovered that the variability is caused by a steep power-law component of $\Gamma \simeq 2.7$, possibly related to non-thermal jet emission. We discuss our findings in the context of similarities and differences between radio-loud/quiet objects.

Key words: galaxies: active — galaxies: individual (3C 120) — galaxies: Seyfert — X-rays: galaxies

1. Introduction

One of the most important issues in the study of active galactic nuclei (AGN) is why well-collimated, powerful, relativistic radio jets exist only in 10% of the AGN class, i.e., in so-called radio-loud objects (e.g., Urry & Padovani 1995).¹ All AGNs are thought to be powered by the accretion of matter onto a supermassive black hole, presumably via an equatorial accretion disk. Recent VLBI observations of a nearby active galaxy, M 87, confirmed that the jet is already launched within $\sim 60 r_g$ (where $r_g = GM/c^2$ is the gravitational radius), with a strong collimation occurring within $\sim 200 r_g$ of the central black hole (Junor et al. 1999). These results are consistent with the hypothesis that jets are formed by an accretion disk, which is threaded by a magnetic field. Therefore, the observational properties of the accretion

disk and corona are essential ingredients to jet formation (e.g., Livio 1999 and references therein).

The profile of the iron $K\alpha$ (6.4 keV) line can be used to probe the structure of the accretion disk, because it is thought to result from fluorescence of the dense gas in the geometrically thin and optically thick regions of the inner accretion disk ($\sim 10 r_g$). The most famous example is the spectrum of the Seyfert 1 (Sy-1) galaxy MCG –6–30–15, which shows a relativistically broadened Fe $K\alpha$ emission line, first detected by ASCA (Tanaka et al. 1995; Iwasawa et al. 1996, 1999). This finding was confirmed by Chandra and XMM-Newton (e.g., Wilms et al. 2001; Fabian et al. 2002), and most recently by Suzaku (Miniutti et al. 2007). Similar broad relativistic iron line profiles have been detected in several other type-1 AGN (e.g., Nandra et al. 1999; Iwasawa et al. 2004; Turner et al. 2005 for NGC 3516; Page et al. 2001 for Mrk 766), although they are perhaps somewhat less common than anticipated from the ASCA era (e.g., Nandra et al. 1997). In contrast, the presence of a narrower 6.4 keV line from more distant matter (e.g., from the outer

¹ More accurately, a well-known dichotomy of the radio-loud and radio-quiet objects is based on the old VLA study of PG quasars (Kellermann et al. 1989), and recent deep VLA FIRST survey shows no such sign of bimodality in radio loudness (White et al. 2000).

Table 1. Suzaku observation log of 3C 120.

Obs_ID	Start (UT)	Stop (UT)	XIS/HXD exposures (ks)
3C 120 #1	2006 Feb 09 03:20	2006 Feb 10 05:50	33.3/29.3
3C 120 #2	2006 Feb 16 13:08	2006 Feb 17 14:06	36.4/32.6
3C 120 #3	2006 Feb 23 20:02	2006 Feb 24 18:00	37.0/36.2
3C 120 #4	2006 Mar 02 22:29	2006 Mar 03 20:39	37.9/37.4

disk, broad/narrow line regions, or torus) is common in many type-1 AGNs (e.g., Yaqoob & Padmanabhan 2004). In this context, studies of the iron line profile in radio-loud AGN provides important clues concerning the disk–jet connection, particularly by comparison with Sy-1s. Moreover, in a standard picture of two-phase disk–corona model proposed by Haardt & Maraschi (1991), the corona temperature is related to the high-energy cutoff typically observed in the hard X-ray band (see also Poutanen & Svensson 1996). Thus, observations of the Compton reflection hump and its cutoff above 10 keV can be used to determine the geometry and temperature of the disk–corona system postulated to exist in both types of AGNs (e.g., Woźniak et al. 1998).

3C 120 ($z = 0.033$) is the brightest broad line radio galaxy (BLRG), exhibiting characteristics intermediate between those of FR-I radio galaxies and BL Lacs. It has a one-sided superluminal jet on 100 kpc scales (Walker et al. 1987; Harris et al. 2004); also, superluminal motion (with an apparent velocity $\beta_{\text{app}} = 8.1$) has been observed for the jet component (Zensus 1989). This provides an upper limit to the inclination angle of the jet to the line of sight of 14° (Eracleous & Halpern 1988). Interestingly, the optical spectrum of 3C 120 is not LINER-like, as is often seen in FR-I radio galaxies (e.g., Baum et al. 1995), but rather typical of Sy-1s. It resides in an optically peculiar galaxy that shows only some indication of a spiral structure (Moles et al. 1988). From reverberation mapping, the central black hole mass is remarkably well constrained: $M = 5.5_{-2.3}^{+3.1} \times 10^7 M_\odot$ (Peterson et al. 2004; see also Wandel et al. 1999). Very recently, Marscher et al. (2002) found that dips in the X-ray emission of 3C 120 are followed by ejections of bright superluminal knots in the radio jet, which clearly indicates an important connection between the jet and the accretion disk.

In X-rays, 3C 120 has been known to be a bright ($\sim 5 \times 10^{-11} \text{ erg cm}^{-2} \text{ s}^{-1}$ at 2–10 keV), variable source with a canonical power-law spectral shape that softened as the source brightened (e.g., Maraschi et al. 1991 and reference therein). A broad iron $K\alpha$ line was first detected by ASCA in 1994, with its width of $\sigma = 0.8 \text{ keV}$ and EW (equivalent width) $\sim 400 \text{ eV}$ (Grandi et al. 1997; Reynolds 1997; Sambruna et al. 1999). Follow-up observations by RXTE (Eracleous et al. 2000; Gliozzi et al. 2003) and BeppoSAX (Zdziarski & Grandi 2001) also detected a broad iron line, but with a much smaller EW of $\sim 100 \text{ eV}$. Furthermore, these observations confirmed the presence of a weak Compton hump in 3C 120, with a reflection normalization of $\Omega/(2\pi) \sim 0.4$. It was argued that both the weak line and the relative weakness of the Compton hump is suggestive of an optically thick accretion disk that transitions

to a hot, optically thin flow (Eracleous et al. 2000; Zdziarski & Grandi 2001). Without a doubt, 3C 120 is a key source to construct a unified view of radio-loud and radio-quiet objects.

Most recently, 3C 120 was observed for nearly a full orbit (130 ks) with XMM-Newton on 2003 August 26–27 (Ballantyne et al. 2004; Ogle et al. 2005). This clearly confirmed the presence of neutral Fe line emission ($57 \pm 7 \text{ eV}$ in EW), which was slightly broadened with a FWHM of $\sigma = 9000 \pm 3000 \text{ km s}^{-1}$. Both of these papers argued that the line profile is rather symmetric, and no evidence was found for relativistic broadening, or alternatively the line arises from an accretion disk radius of $\geq 75 r_g$ at an inclination angle of $\sim 10^\circ$ (where relativistic gravitational effects are almost negligible). They also confirmed a weaker emission line at 6.9 keV with $EW = 20 \pm 7 \text{ eV}$ (initially suggested by Chandra HETGS; Yaqoob & Padmanabhan 2004), which can be interpreted as being a blend of Fe $K\beta$ and H-like (or He-like) iron lines. Despite significant progress made by XMM-Newton, most of the results are not conclusive, due to XMM-Newton’s limited energy range (no coverage above 10 keV), and the relatively high background of XMM-Newton above 5 keV. At present, various models can fit these iron lines equally well, though they assume quite different geometries and/or ionization states (Ballantyne et al. 2004; Ogle et al. 2005). It has been argued that such degeneracies may be resolved by Suzaku, due to its unprecedented sensitivity between 0.3 and $\sim 300 \text{ keV}$.

In this paper, we present a detailed analysis of 160 ks worth of data on 3C 120, observed with Suzaku in 2006 February and March as a part of the SWG (science working group) program. Since our aim was to monitor the source in various states of source activity, we divided this total exposure into four exposures of 40 ks each, with one pointing per week (to be roughly equal to the variability timescale of this source; e.g., Marshall et al. 2003; Gliozzi et al. 2003). Thanks to the excellent energy resolution and sensitivity of the XIS and HXD/PIN onboard Suzaku, we successfully obtained one of the highest quality data on this radio galaxy ever reported, between 0.6 and 50 keV. The paper is organized as follows. The observation and analysis methods are described in section 2. We present an overview of 3C 120’s variability during the Suzaku observations and temporal studies of light curves in section 3. Detailed spectral studies are presented in section 4; in particular we focus on (1) multiband spectral features, (2) the nature of the iron K line complex, and (3) the difference spectrum between high and low states. Based on these new findings, we discuss the nature of the variability and spectral evolution of 3C 120 in section 5. Finally, we present our conclusions in section 6. Uncertainties of background models on the HXD/PIN light curve are discussed further in

detail in the appendix.

2. Observation and Data Reduction

The broad line-radio galaxy 3C 120 was observed with Suzaku (Mitsuda et al. 2007) four times in 2006 February and March with a total (requested) duration of 160 ks. Table 1 summarizes the start time and the end time, and the exposures of each observation. Suzaku carries four sets of X-ray telescopes (Serlemitsos et al. 2007), each with a focal-plane X-ray CCD camera (XIS, X-ray Imaging Spectrometer; Koyama et al. 2007) that is sensitive in the energy range of 0.3–12 keV, together with a non-imaging Hard X-ray Detector (HXD; Takahashi et al. 2007; Kokubun et al. 2007), which covers the 10–600 keV energy band with Si PIN photo-diodes and GSO scintillation detectors. Three of the XIS (XIS 0, 2, 3) have front-illuminated (FI) CCDs, while the XIS 1 utilizes a back-illuminated (BI) CCD. The merit of the BI CCD is its improved sensitivity in the soft X-ray energy band below 1 keV. In all four observations (3C 120 #1–#4), 3C 120 was focused on the nominal center position of the XIS detector.

2.1. XIS Data Reduction and Analysis

For the XIS, we analyzed version 0.7 of the screened data (Fujimoto et al. 2007) provided by the Suzaku team. The screening of the version 0.7 data was based on the following criteria: (1) only ASCA-grade 0, 2, 3, 4, 6 events (Yamaguchi et al. 2006) are accumulated, while hot and flickering pixels were removed from the XIS image using the CLEANIS script, (2) the time interval after the passage of South Atlantic Anomaly (T_{SAA}) is larger than 436 s, (3) the object is at least 5° and 20° above the rim of the Earth (ELV) during night and day, respectively. In addition, we also select the data with a cutoff rigidity (COR) larger than 6 GV. The XIS events were extracted from a circular region with a radius of 4'3 centered on the source peak, whereas the background was accumulated in an annulus with its inner and outer radii of 4'9 and 6'6, respectively. For the 3C 120 #3 observation (see table 1), we discarded the first 600 s data after the maneuver because the pointing fluctuated from its center (i.e., XIS nominal position) by $\sim 2'$.

The XIS spectra were corrected for the hydrocarbon (C₂₄H₃₈O₄) contamination on the optical blocking filter, by including an extra absorption column due to carbon and oxygen in all of the spectral fits. The column densities for each detector were calculated based on the date of the observation using an empirical relation released by the Suzaku instrumental team. We assumed different carbon and oxygen column densities (N_C and N_O) for different sensors and observations: $N_C = (2.38\text{--}2.56)\times 10^{18}$, $(3.20\text{--}3.50)\times 10^{18}$, $(3.65\text{--}3.80)\times 10^{18}$, and $(5.44\text{--}5.65)\times 10^{18}$ atoms cm⁻² for XIS 0, 1, 2, 3 respectively, with the ratio of C/O column densities (N_C/N_O) set to 6. This additional soft X-ray absorption due to the hydrocarbon contamination was included as a fixed spectral component using the VARABS absorption model in all of the spectral fits.

Although 3C 120 is known to have a large extended X-ray jet that is $\sim 20''$ apart from the nucleus (Harris et al. 2004), and could not be resolved with Suzaku, the X-ray contribution from this large-scale (10kpc scale) jet

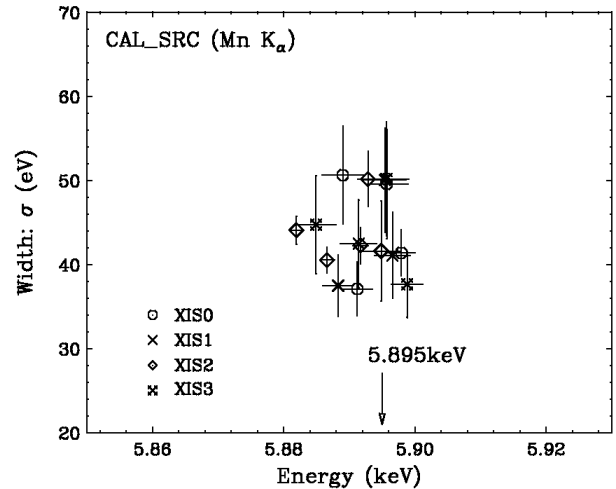


Fig. 1. Energy scale and residual width of the ⁵⁵Fe calibration source on each of the XIS sensors, during each of the four observations.

is less than 1% of the nucleus emission in the 0.5–10 keV bandpass ($F_{\text{jet}} \sim 2.3 \times 10^{-13}$ erg cm⁻² s⁻¹). We therefore used the latest version of both the response matrix and the point spread function (PSF) released by the Suzaku team for the point-like sources, ae_xi[0,1,2,3]_20060213.rmf and ae_xi[0,2,3]_xisnom6_20060415.arf. Since the nuclear emission is very bright from 0.5–10 keV, we binned the XIS spectra to a minimum of 200 counts per bin to enable the use of the χ^2 minimization statistic.

Another note on the XIS data analysis is the accuracy of the energy scale (reported to be less than 0.2%, Koyama et al. 2007) and the energy resolution. These calibrations are very important because one of our ultimate goals is to obtain precise measurements of the iron line complex, as discussed see in subsection 4.3. For this purpose, an ⁵⁵Fe calibration source located on the corners of the XIS chips was used as an accurate calibrator of the instrumental response during 3C 120 observations.² The ⁵⁵Fe source produced a characteristic X-ray line from Mn K α at 5.895 keV (a combination of K α 1 and K α 2 at 5.899 keV and 5.888 keV, respectively, with a branching ratio of 2 : 1). Figure 1 shows the results of Gaussian fitting for each of the XIS chips during 3C 120 observations #1–#4.

From measuring the 5.895 keV lines in the calibration source, we found that the line energy is shifted slightly redwards by 5.5 ± 0.6 eV, while there is some residual width (after the instrumental response function has been accounted for) in the calibration lines of $\sigma_{\text{cal}} = 45 \pm 1$ eV. A further check of the line width was made by using Sgr C (molecular cloud) data that was taken between 3C 120 #2 and #3. As reported in Ueno et al. (2007), the 1 σ width of the 6.4 keV line in the Sgr C observation was 39 ± 5 eV, which is consistent with the 3C 120 calibration lines within the statistical error. Since the intrinsic line width is expected to be negligible for this

² Note the ⁵⁵Fe calibration source is on the corners of the XIS chips, while 3C 120 is focused on the center of the CCD. From a detailed analysis of galaxy clusters and Sgr C, the XIS team confirmed that this position difference makes only negligible effects in both the line width and spatial gain variations.

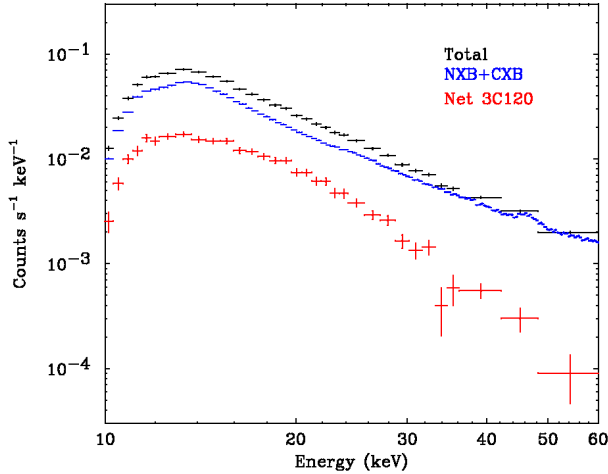


Fig. 2. The combined HXD/PIN spectrum for the Suzaku observation of 3C 120 #1–#4 over the whole HXD/PIN energy bandpass (10–60 keV). Upper plus (black) shows the total spectrum (source plus background), middle (blue) shows sum of non-X-ray background and the CXB, and lower plus (red) for the net source spectrum. Note the source is detected in each data bin at more than 10% of background level over the 12–50 keV range used in this paper.)

molecular cloud, it must be mostly instrumental. Therefore, in the following, the intrinsic width of the iron $K\alpha$ line is simply evaluated as $\sigma_{\text{int}} = \sqrt{\sigma_{\text{obs}}^2 - \sigma_{\text{cal}}^2}$, where σ_{obs} is the measured width of the iron line discussed below.

2.2. HXD Data Reduction and Analysis

The source spectrum and the light curves were extracted from the cleaned HXD/PIN event files (version 1.2) provided by the Suzaku team. The HXD/PIN data are processed along with the screening criteria, being basically the same as that for the XIS, except that $\text{ELV} \geq 5^\circ$ through night and day, $T_{\text{SAA}} \geq 500$ s, and $\text{COR} \geq 8$ GV. The HXD/PIN instrumental background spectra were generated from a time dependent model provided by the HXD instrument team for each observation. The model utilized the count rate of the upper discriminators and the COR values as a measure of the cosmic-ray flux that passes through the Si PIN diode; background spectra based on a database of non-X-ray background observations made by the PIN diode to date are provided (see Kokubun et al. 2007; Fukazawa et al. 2006 for more details). At the time of writing, two different background models, A and B, were under investigation, but the difference between the two models is rather small for our 3C 120 HXD/PIN data analysis. According to careful examinations using simulations on various observational datasets, the uncertainty of the background models for the PIN detector is expected to be $\sim 5\%$ for both models A and B (see Appendix).

Both the source and the background spectra were made with identical GTIs (good time intervals) and the exposure was corrected for a detector deadtime of $\sim 5\%$ (ranges in 3.5–8.5% for 3C 120 observations; see Appendix). To minimize any uncertainties due to limited photon statistics on the background models, background spectra were generated

with 10 times the actual background count rate, but increasing the effective exposure time of the background by a factor of 10. The HXD/PIN response file, dated 2006-08-14 for the XIS nominal position (ae_hxd_pininom_20060814.rsp), was used for these spectral fits. Full details of the HXD instrument and the performance are given in Takahashi et al. (2007) and Kokubun et al. (2007).

The time-averaged (obs #1–#4 combined) HXD/PIN spectrum is shown in figure 2, plotted over the energy range of 10 to 60 keV. HXD/PIN data below 12 keV have been ignored to avoid noise contamination near the lower threshold of the PIN diode. Also the data above 50 keV are discarded, as a detailed study of noise and background systematics is on-going above this energy. Figure 2 shows the total (3C 120 + observed background) spectrum, where the background includes both the instrumental (non-X-ray) background model-A and the contribution from the cosmic X-ray background (CXB) (Gruber et al. 1999). Here, the form of the CXB was taken as $9.0 \times 10^{-9} (E/3 \text{ keV})^{-0.29} \times \exp(-E/40 \text{ keV}) \text{ erg cm}^{-2} \text{ s}^{-1} \text{ keV}^{-1}$ and the observed spectrum was simulated assuming the PIN detector response to isotropic diffuse emission. When normalized to the field of view of the HXD/PIN instrument, the effective flux of the CXB component is expected to be $9.0 \times 10^{-12} \text{ erg cm}^{-2} \text{ s}^{-1}$ in the 12–50 keV band, which is about $\sim 14\%$ of the 3C 120 flux in the same energy bandpass.

3C 120 is known to have a 50–100 keV flux of $\sim 5 \times 10^{-11} \text{ erg cm}^{-2} \text{ s}^{-1}$ (e.g., Woźniak et al. 1998; Zdziarski & Grandi 2001), and therefore can ultimately be detected by the HXD/GSO detector. However, this is only a few percent of the GSO detector background, and a study at this level of background systematics is still on-going by the HXD instrumental team. Therefore, in this paper we do not include the GSO data in the subsequent spectral fits. Above 50 keV, a reliable detection of 3C 120 cannot be made at the present time by the GSO, but results using new response matrices and revised background models will be discussed elsewhere in the near future.

3. Temporal Studies

3.1. Overview of Variability

Figure 3 shows an overview of the count rate variations of 3C 120 during the February and March observations (#1–#4). The light curves of the 4 XISs and PIN detectors are shown separately in different energy bands: 0.4–2 keV (upper, XIS), 2–10 keV (middle, XIS), and 12–40 keV (lower, HXD/PIN). The net source count rates, averaged over four observations, measured from 0.4–10 keV were $2.965 \pm 0.005 \text{ cts s}^{-1}$, $3.703 \pm 0.005 \text{ cts s}^{-1}$, $2.972 \pm 0.005 \text{ cts s}^{-1}$, and $2.799 \pm 0.005 \text{ cts s}^{-1}$, respectively for the XIS 0, 1, 2, 3. The background is typically 3% of the source counts for the FI-XIS (XIS 0, 2, 3) and 7% for the BI-XIS (XIS 1). For the PIN detector, the net average source count rate in the 12–40 keV band was $0.150 \pm 0.002 \text{ cts s}^{-1}$, compared to the PIN background (non-X-ray background + CXB) rate of 0.449 cts s^{-1} .

Figure 3 clearly indicates that 3C 120 was in a relatively high state during the 1st 40 ks observation (#1; the summed

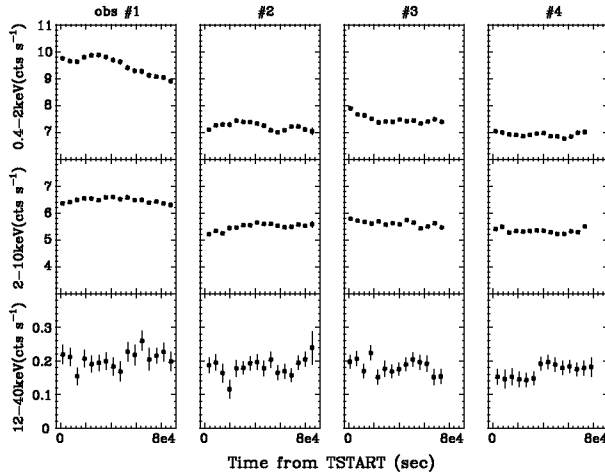


Fig. 3. Overall variability of 3C 120 during 2006 February and March observations by Suzaku. upper: 0.4–2 keV XIS (XIS 0–3 summed), middle: 2–10 keV XIS (XIS 0–3 summed), and lower: 12–40 keV XIS (XIS 0–3 summed). The backgrounds are subtracted.

count rates of 4 XISs detectors was 15.94 ± 0.01 cts s^{-1}); its count rate then dropped by $\sim 20\%$ in the 2nd observation, and finally reached a minimum in the 4th observation (#4; 12.02 ± 0.01 cts s^{-1}). Here, the effect of a time dependent degradation of the XIS efficiency due to C and O contamination (Koyama et al. 2007; see also subsection 2.1) was corrected between 3C 120 #1 and #4, though this had only a negligible effect, even below 2 keV within one-month scale. Interestingly, a large time variation of the 0.4–2 keV count rate in the 1st observation was not clearly detected above 2 keV, suggesting a relative lack of variability at higher energies, as had already been noticed for this particular source by various authors (e.g., Maraschi et al. 1991; Zdziarski & Grandi 2001). The count-rate variations of the HXD/PIN detector were less clear due to limited photon statistics, but some level of variability existed, as we discuss in the next section.

3.2. Hardness Ratio

Figure 4 (upper) compares the XIS count-rate correlation between the soft X-ray (0.4–2.0 keV) and hard X-ray energy bands (2–10 keV). Generally, the correlation is tight, such that hard X-ray flux increases when the soft X-ray flux increases. However, some scatter in the correlation suggests some variation of the spectrum, even if the source is in similar flux states. Moreover, the amplitude of flux variations is approximately 40% in 0.4–2 keV, but only $\sim 25\%$ in 2–10 keV. Figure 4 (lower) shows the soft X-ray count rates (0.4–2 keV) versus the hardness ratio, where the hardness is defined as 2–10 keV count rates divided by 0.4–2 keV count rates. This clearly suggests a spectral evolution such that the spectrum becomes softer when the source becomes brighter; but again, the correlation is rather loose, especially when the source is in lower states of activity (obs #2–#4). Also, it appears that the hardness diagram cannot be fit linearly against 0.4–2 keV source counts. This may suggest that more than just one spectral component is

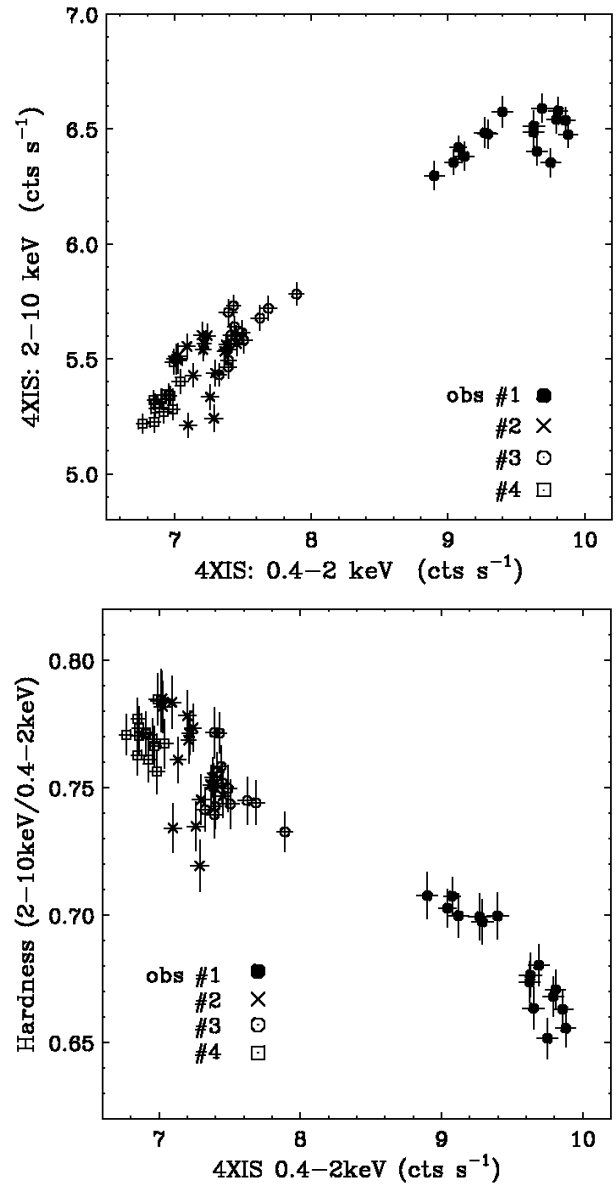


Fig. 4. Upper: Correlation of XIS count rates between 0.4–2 keV and 2–10 keV. Lower: Changes of hardness ratio between 0.4–2 keV and 2–10 keV. The hardness is defined as 2–10 keV count rates divided by 0.4–2 keV count rates.

responsible for the 3C 120 X-ray emission.

Similarly figure 5 (upper) compares the 2–10 keV XIS and 12–40 keV HXD/PIN count rates during the 3C 120 #1–#4 observations. Again, one can find a weak correlation between source variability in these two energy bands. In this particular case, however, the hardness seems to stay almost constant within the statistical errors, as shown in figure 4 (lower). The apparent small changes in the hardness ratio may suggest a relative lack of spectral evolution above 2 keV, though hardness changes of $\sim 20\%$ level [as observed in figure 4 (upper)] are difficult to detect above 10 keV, due to limited photon statistics.

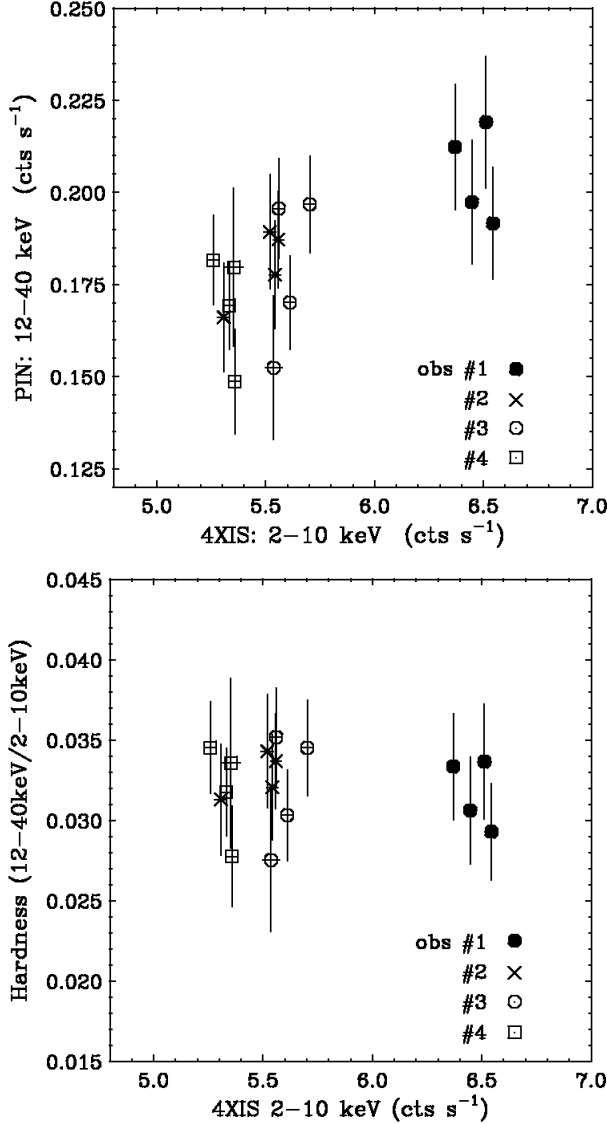


Fig. 5. Upper: Correlation of count rates between 2–10 keV (XISs) and 12–40 keV (HXD/PIN). Lower: Changes of hardness ratio. The hardness is defined as the 12–40 keV count rate divided by the 2–10 keV count rate.

3.3. Excess Variance

For more detailed temporal studies, obs #1–#4 light curves are further divided into 6 energy bands (0.4–1 keV, 1–2 keV, 2–3 keV, 3–5 keV, 5–7 keV, 7–10 keV) for the XISs and 1 energy bands (12–40 keV) for the HXD/PIN, respectively. To estimate the amplitude of variability in a systematic way, “excess variance” (e.g., Zhang et al. 2002 and reference therein), was calculated for light curves derived in different energy bands. The excess variance (σ_{rms}^2) is a net variance, which is defined as the difference between the total variance (σ_{tot}^2) and the noise variance (σ_{noise}^2), which is caused by statistical errors,

$$\sigma_{\text{rms}}^2 = \frac{1}{N\bar{x}^2} \sum_{i=1}^N [(x_i - \bar{x})^2 - \sigma_i^2] = \frac{1}{\bar{x}^2} (\sigma_{\text{tot}}^2 - \sigma_{\text{noise}}^2), \quad (1)$$

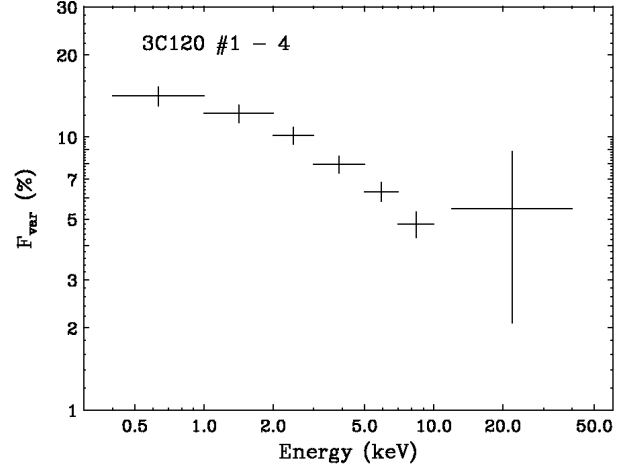


Fig. 6. Energy dependence of variability of 3C 120 #1–#4. The variability parameter, excess variance, was calculated for the total exposure in 7 (6 for 4 XISs + 1 for HXD/PIN) energy bands. The HXD/PIN data where the background is high (photon counts of ≥ 0.7 cts s⁻¹) were not used to minimize the uncertainty due to background subtraction (see Appendix).

where x_i is the i -th bin in the light curve and \bar{x} is the mean of x_i . The error on σ_{rms}^2 is estimated by $s_D/(\bar{x}^2\sqrt{N})$, where s_D is the variance of the quantity $(x_i - \bar{x})^2 - \sigma_i^2$ and given by (Turner et al. 1999)

$$s_D^2 = \frac{1}{N-1} \sum_{i=1}^N \{[(x_i - \bar{x})^2 - \sigma_i^2] - \sigma_{\text{rms}}^2 \bar{x}^2\}^2. \quad (2)$$

The fractional variability parameter F_{var} used in this paper is the square root of excess variance: $F_{\text{var}} = (\sigma_{\text{rms}}^2)^{1/2}$.

Figure 6 shows F_{var} measured in this way, using the overall light curves combined in obs #1–#4. Again, we carefully consider the effect of time dependent degradation of the XIS efficiency, but it only accounts for an $\sim 2\%$ decrease of the XIS count rates, even in 0.4–1.0 keV band. Clearly, the variability is larger in the lower energy bands; the largest variability was observed in the 0.4–1 keV band with $F_{\text{var}} = 14.1 \pm 1.1\%$, and it gradually decreased with increasing energy, and reached $4.8 \pm 0.5\%$ at 7–10 keV. The variability amplitude above 10 keV cannot be well constrained ($F_{\text{var}} = 5.5 \pm 3.4\%$), but is consistent with those of the 7–10 keV variability observed with the XIS. Note this range of variability is consistent with that reported in Markowitz and Edelson (2004), who found $F_{\text{var}} = 6\%$ on 6-day time scales and 8% on 36-day time scale in 2–12 keV. We also calculated the excess variance of the light curves accumulated within each of the 40 ks observations (obs #1, #2, #3, #4, respectively). The amplitude was smaller on this shorter time scale, with $F_{\text{var}} \leq 3\%$ in all energy bands, and sometimes consistent with no variability. We therefore conclude that the variability time scale of 3C 120 is much larger than one day, typically $t_{\text{var}} \sim 10^6$ s. This relatively long timescale of variability is consistent with those found in literature (e.g., Marshall et al. 2003; Gliozzi et al. 2003; also see the Appendix for apparent short-term variations seen in the HXD/PIN light curve).

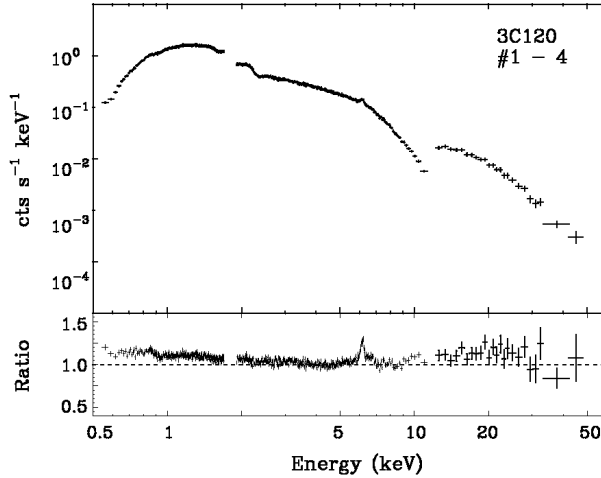


Fig. 7. Broad-band (0.6–50 keV; 3 FI-XISs + PIN) Suzaku spectrum of 3C 120. The upper panel shows the data, plotted against an absorbed power-law model of photon index $\Gamma = 1.74$ and column density $1.23 \times 10^{21} \text{ cm}^{-2}$, fitted over the 4–12 keV band. The lower panel shows the data/model ratio residuals to this power-law fit. Deviations due to (1) the iron K-shell band, (2) the Compton reflection hump, and (3) excess soft emission are clearly seen.

4. Spectral Studies

4.1. Overview of the Broad-Band Spectrum

Before going into a detailed spectral study, we quickly overview the time-averaged spectrum of 3C 120 between 0.6 and 50 keV, from the whole Suzaku observation (obs #1–#4 combined). The XIS and HXD/PIN background-subtracted spectra were fitted using XSPEC v11.3.2p, including data over the energy range the 0.6–50 keV. The Galactic absorption toward 3C 120 is taken to be $N_{\text{H}} = 1.23 \times 10^{21} \text{ cm}^{-2}$ (Elvis et al. 1989). All errors are quoted at the 68.3% (1 σ) confidence for one interesting parameter, unless otherwise stated. All of the fits mentioned in this section are restricted to within the energy range of 0.6–12 keV (XIS 0, 2, 3: FI chips), 0.6–10 keV (XIS 1: BI chip), and 12–50 keV (HXD/PIN).

As a first step, we fitted the 4 XIS spectra using a simple absorbed power-law model in the 3–10 keV band, excluding 5–7 keV, in order for the continuum parameters not to be affected by possible iron line features, absorption/excess features in the lower energy band, as well as the reflection component expected to be present above 10 keV. Since we found that the spectral parameters of the 4 XIS spectra are all in good agreement within the error bars (at the few percent level), data from 3 FI-XISs (XIS 0, 2, 3) were co-added to maximize the signal-to-noise ratio. Figure 7 shows the 4 XISs + HXD/PIN spectra with residuals to this baseline model, where the XIS data around the Si K edge from 1.7–1.9 keV were discarded in all 4 XIS chips, due to uncertain calibration at this energy at the time of this writing. We also did not use the data below 0.6 keV, as uncertainties in C/O contamination are more significant (see subsection 2.1).³

³ We note, an uncertainty in the calibration affects only the “spectral shape” around the Si K edge. Similarly, the XIS spectra below 0.6 keV is still

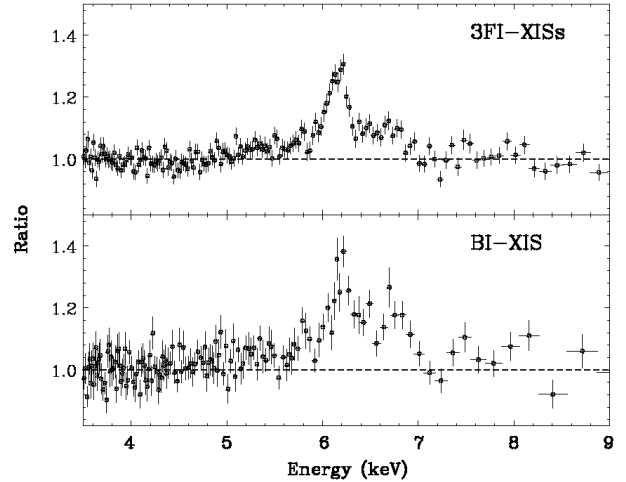


Fig. 8. Zoom-in of the iron line profile of 3C 120, plotted as a ratio against a power-law of photon index of $\Gamma = 1.74$. (upper): XIS 0, 2, 3 combined, (lower): XIS 1.

The best fit spectral power-law index thus determined was $\Gamma = 1.74$, but was statistically unacceptable if we extrapolate the model to lower and higher energies ($\chi^2/\text{d.o.f} = 6593/614$). The residuals of figure 7 shows that the spectrum exhibits features at different X-ray energies: (1) iron-line features around 6 keV, (2) a hard X-ray bump above 10 keV, and (3) excess emission below 3 keV. In particular, the structure around the iron K emission line is rather more complicated than that inferred from any previous X-ray satellite. A zoom-in of the “iron-line complex” observed with Suzaku is presented, respectively, for the FI-XISs and BI-XIS in figure 8. Note the asymmetric line profile and the presence of a red-tail below 6 keV.

4.2. The Baseline Continuum Emission

To model the overall X-ray spectrum between 0.6 and 50 keV, we start from the shape of the baseline continuum emission. As for many radio-quiet AGNs, it has been suggested that the continuum of 3C 120 is composed of a direct (primary) power-law plus reflection by cold matter surrounding the nucleus (e.g., Woźniak et al. 1998; Zdziarski & Grandi 2001). We assumed a primary component including an exponential cut-off at high energies of the form $\propto E^{-\Gamma} \times e^{-E/E_{\text{fold}}}$, where E_{fold} is the cut-off energy in keV, Γ is the differential spectral photon index. Furthermore, a reflection component produced by Compton down-scattering of X-rays off neutral material was included, using the PEXRAV model within XSPEC (Magdziarz & Zdziarski 1995). The inclination angle i , was fixed at $18^\circ 2$, which is the minimum allowed by the models, and also close to the limit derived from the superluminal motion of jet; see section 1. The solid angle Ω subtended by the Compton reflector was allowed to vary, and was determined by the parameter $R = \Omega/(2\pi)$.

In this modeling, we fixed the Fe abundance, A_{Fe} , at unity, following approaches previously made for this objects

uncertain due to the C/O contamination, but no problems arises for the temporal studies, as we have presented in section 3.

Table 2. Results of spectral fits to the 3–50 keV XISs + PIN time-averaged, co-added continuum spectrum of 3C 120.*

Model	Γ	E_{fold} [keV]	R [$\Omega/(2\pi)$]	Abundance	i [$^\circ$]	$F_{3-10\text{keV}}^\ddagger$	$F_{10-50\text{keV}}^\S$	$\chi^2/\text{d.o.f}$
PRV [†]	$1.73^{+0.03}_{-0.02}$	100	$0.47^{+0.27}_{-0.12}$	1.0	18.2	30.0 ± 0.1	62.1 ± 0.6	1112/1060

* The 4 XISs data below 3 keV (soft excess) and between 5–7 keV (Fe-line complex) were discarded to avoid the complexity of the models.

[†] PEXRAV model in XSPEC (Magdziarz & Zdziarski 1995). We fixed the cutoff power-law energy $E_{\text{fold}} = 100$ keV and iron abundance $A_{\text{Fe}} = 1.0$.

[‡] 3–10 keV flux in units of 10^{-12} erg cm^{-2} s^{-1} .

[§] 10–50 keV flux in units of 10^{-12} erg cm^{-2} s^{-1} . Constant fraction factor between HXD and XIS was set to be $N_{\text{PIN}}/N_{\text{XIS}} = 1.114^{+0.042}_{-0.079}$ (see also figure 9).

^{||} Parameters fixed to these values.

in the literature (e.g., Ballantyne et al. 2004; Ogle et al. 2005). Similarly, we assumed a fixed value of $E_{\text{fold}} = 100$ keV because the HXD/PIN is not sensitive above 60 keV, and therefore cannot determine the high-energy end of the direct power-law component [in this context, see Woźniak et al. (1998) who confirmed a cutoff with $E_{\text{fold}} \sim 100$ keV at a significance of 99.95% by combined ASCA and OSSE analysis. Ballantyne et al. (2004) assumed a fixed E_{fold} of 150 keV to fit a combined XMM-Newton and RXTE/HEXTE spectrum. Also, Zdziarski and Grandi (2000) found $E_{\text{fold}} \sim 120$ –150 keV using the Beppo-SAX data].

As a first step, we fit the combined XIS + HXD/PIN data only above 3 keV, since the data below this energy are significantly contaminated by the soft excess emission, as we have shown in figure 7. Similarly, data between 5 and 7 keV was ignored so as to avoid the region around the iron line complex. Even with this simplified model and constrained parameters, special care must be paid to the cross calibration of the XIS and the HXD/PIN, because it could easily affect the determination of the reflection parameter, R . At the date of writing (2006 November), the relative normalization of the HXD/PIN was reported to be 1.13-times larger than the XIS, as determined by the XRT team using the spectrum of the Crab Nebula (M. Ishida, JX-ISAS-Suzaku-memo 2006-40).

Figure 9 shows the confidence contours of reflection parameter, $R = \Omega/(2\pi)$, against the relative normalization of the XISs/PIN. An apparent anti-correlation between the two parameters indicates that R is strongly affected by the normalization factor between the two instruments. Nevertheless, the mean value of normalization factor ($1.114^{+0.042}_{-0.079}$) is perfectly consistent with that determined from the Crab Nebula, and the reflection parameter is well constrained at $R = 0.47^{+0.27}_{-0.12}$. The resultant parameters for the baseline continuum emission are summarized in table 2. The photon index of the direct component was determined to be $\Gamma = 1.73^{+0.03}_{-0.02}$. The observed flux of the continuum emission (direct + reflection) is $(30.0 \pm 0.1) \times 10^{-12}$ erg cm^{-2} s^{-1} over 3–10 keV, and $(62.1 \pm 0.6) \times 10^{-12}$ erg cm^{-2} s^{-1} over 10–50 keV.

Finally, we comment on how the results are affected if we choose different values of A_{Fe} and E_{fold} , which are unfortunately still uncertain, even when using the Suzaku data. We are aware that fixing these parameters is

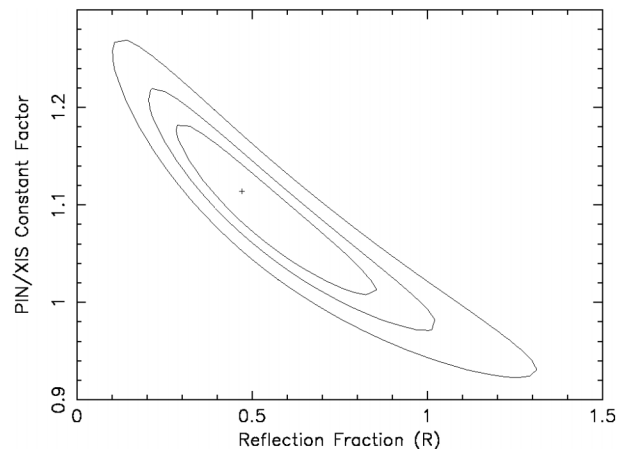


Fig. 9. Contour plot showing the reflection parameter, R , versus the constant normalization factor between the HXD/PIN and XIS, which shows that the constant factor (defined here as $N_{\text{HXD/PIN}}/N_{\text{XIS}}$, where N is the normalization) is close to 1.1, which is consistent with the cross calibration between the XIS and the HXD using the Crab Nebula. Confidence levels in the figure correspond to the 68%, 90%, and 99% levels of significance, respectively.

an oversimplification because both A_{Fe} and E_{fold} could vary depending on the reflection parameter, R . Using a fixed value of $E_{\text{fold}} = 100$ keV, both the reflection parameter and the power-law photon index are only slightly affected, where the best-fit values provide $1.70 \leq \Gamma \leq 1.76$ and $0.43 \leq R \leq 0.53$, respectively, for a range of $0.5 \leq A_{\text{Fe}} \leq 2.0$. If we set $E_{\text{fold}} = 50$ keV, the reflection parameter becomes slightly large ($0.77 \leq R \leq 0.97$ for $0.5 \leq A_{\text{Fe}} \leq 2.0$), but statistically not significantly different. The power-law photon index is within a range of $1.70 \leq \Gamma \leq 1.76$. Similarly, a different choice of $E_{\text{fold}} = 150$ keV provides $0.37 \leq R \leq 0.45$ for $0.5 \leq A_{\text{Fe}} \leq 2.0$, with $1.72 \leq \Gamma \leq 1.76$. Again, these are relatively small effects, and thus we assume $A_{\text{Fe}} = 1.0$ and $E_{\text{fold}} = 100$ keV in the following analysis.

4.3. Iron Line Complex

4.3.1. Line profile

We next consider the X-ray spectrum of 3C 120 between 3 and 10 keV, with inclusion of the 5–7 keV data. The iron K line profile was then fitted in several steps. Firstly, we

Table 3. Results of spectral fits.*

Model	E_1 [keV]	σ_1^{\parallel} (EW) [eV]	E_2 [keV]	σ_2^{\parallel} (EW) [eV]	E_{DL} [keV]	r_{in} [r_g]	i [$^{\circ}$]	χ^2 (d.o.f)
1. PRV [†]	2500 (1606)
2. PRV [†] +G [‡]	$6.378^{+0.013}_{-0.009}$	193^{+32}_{-31} (101^{+17}_{-16})	1807 (1603)
3. PRV+DL [§]	$6.390^{+0.007}_{-0.009}$	$40.7^{+6.9}_{-5.0}$	18.2**	1853 (1603)
4. PRV+2G	6.373 ± 0.009	158^{+15}_{-17} (90^{+9}_{-10})	6.93 ± 0.02	10** (18)	1757 (1601)
5. PRV+G+DL	$6.368^{+0.008}_{-0.006}$	69^{+6}_{-8} (49^{+5}_{-6})	$6.41^{+0.10}_{-0.06}$	$19.4^{+5.1}_{-1.8}$	$49.7^{+1.9}_{-7.1}$	1691 (1599)
6. PRV+2G+DL	6.398 ± 0.01	111^{+11}_{-10} (60 ± 6)	6.93 ± 0.02	10** (17)	6.40^{**}	$8.6^{+1.0}_{-0.6}$	$6.5^{+3.8}_{-3.2}$	1681 (1598)

* The fits to the 3–10 keV XIS 0–3 time-averaged, co-added spectrum with the different models used to describe the Fe-line complex of 3C 120.

[†] PEXRAV model in XSPEC (Magdziarz & Zdziarski 1995). We assumed the direct power-law of $\Gamma = 1.73$ with 3–10 keV flux $F_{3-10 \text{ keV}} = 3.0 \times 10^{-11} \text{ erg cm}^{-2} \text{ s}^{-1}$ (see table 2). We fixed the reflection parameter $R = 0.47$ and Fe abundance $A_{Fe} = 1.0$.

[‡] A simple Gauss function in XSPEC modified by redshift of 3C 120.

[§] DISKLINE model assuming a power-law dependence of emissivity, $\beta = -3.0$.

^{||} An intrinsic width of iron line (excluding residual width in calibration $\sigma_{cal} = 45 \pm 1 \text{ eV}$; see subsection 2.1).

[#] 3–10 keV flux in units of $10^{-12} \text{ erg cm}^{-2} \text{ s}^{-1}$.

** Parameters fixed to these values.

fit the joint FI-XISs (XIS 0, 2, 3) and BI-XIS (XIS 1) hard X-ray spectra with the best-fit power-law plus reflection model (PEXRAV: PRV) as described in the previous section. The fit is very poor, as shown in figure 10a and table 3 ($\chi^2_v = 2500/1606 = 1.56$: model 1 in table 3), mostly due to a prominent line profile near 6.2 keV in the observed frame ($\sim 6.4 \text{ keV}$ in the rest frame). Then, adding a single Gaussian Fe $K\alpha$ line to the model (PRV+G) gives a greatly improved fit statistic ($\chi^2_v = 1807/1603 = 1.13$: model 2). The line energy, converted into the rest frame, is $6.378^{+0.013}_{-0.009} \text{ keV}$, indicating neutral or low-ionization Fe. The measured width of the line is $\sigma_{obs} = 193^{+32}_{-31} \text{ eV}$, and the equivalent width is $EW = 101^{+17}_{-16} \text{ eV}$. For completeness, we also added a small Compton shoulder to the iron $K\alpha$ line, represented by a narrow Gaussian profile centered at 6.24 keV, with the normalization fixed to 20% of the $K\alpha$ flux (Matt 2000); but there was no improvement to the fit at 90% confidence (no significant improvement in χ^2).

After inclusion of the iron K line, there still remained a clear excess of photon counts in the Suzaku data between 5 and 7 keV (figure 10b). We further tried to improve the fit by assuming a redshifted diskline rather than a simple Gaussian function (PRV + DL: model 3), or by adding another Gaussian to the model (PRV + 2G; model 4). Indeed, the latter model (model 4) is suggested to fit the XMM-Newton data fairly well (Ogle et al. 2005), and also improves the χ^2 statistics of the Suzaku data significantly ($\chi^2_v = 1757/1601 = 1.10$). However, the inclusion of an additional Gaussian still does not represent very well the “red tail” below 6 keV observed in the

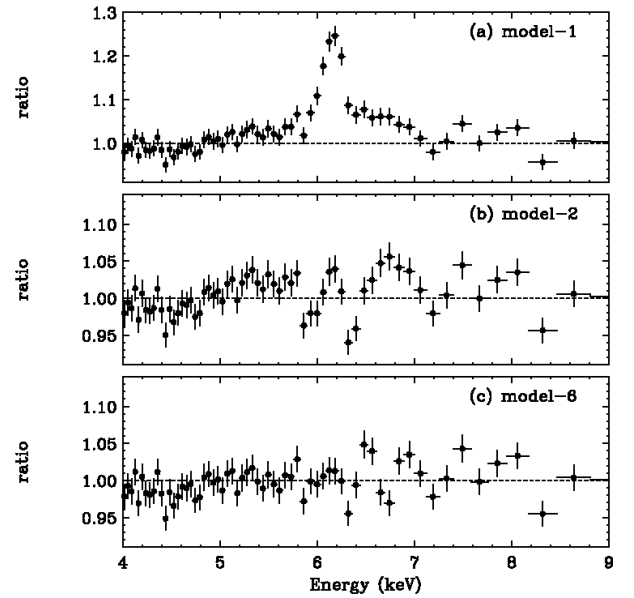


Fig. 10. Data/model ratio residuals of the 3 FI-XISs spectrum of 3C 120 between 4–9 keV. (a) Residual after fitting a power-law ($\Gamma = 1.73$) with a reflection component ($R = 0.47$: model 1 in table 3). (b) Residuals after inclusion of the narrow $K\alpha$ core (model 2 in table 3). (c) Residuals after the addition of a broad diskline emission centered at 6.4 keV, as well as a 6.9 keV line (model 6 in table 3).

Suzaku data. Instead, the inclusion of a broad diskline from an accretion disk (Fabian et al. 1989; see also Reeves et al. 2007 to fit the similar iron line profile of MCG -5-23-16) provides a better representation of the data. As a result, the fit statistics of our “best-fit” model (PRV+G+DL) was improved to $\chi^2_{\nu} = 1691/1599 = 1.06$ (model 5). This “PRV+G+DL” model (model 5), however, predicts a large inclination angle of $i \simeq 50^\circ$. This seems to be problematic when taking into account the tight constraints on the jet inclination angle of $i \leq 14^\circ$ from the superluminal motion, unless the jet is significantly “warped” between the disk and the VLBI (i.e., pc scale) region. Also note that the centroid energy of the Fe line core is $6.368^{+0.008}_{-0.006}$ keV, which is shifted redwards by ~ 30 eV compared to what is expected from a neutral iron $K\alpha$ line (6.400 keV). This shift is effectively larger than the uncertainties in the energy scale determined by the calibration sources (see subsection 2.1).

We therefore considered whether we could fit the same line profile differently, to achieve a more face-on orientation. Basically, the high inclination angle is driven from fitting the blue wing of the line above 6.4 keV. If we assumed there is ionized emission from either He-like (6.7 keV) or H-like (6.97 keV) Fe $K\alpha$ as was suggested in the Chandra HETGS and the XMM-Newton observations, that would reduce the inclination, as the blue wing of the disk line would not need to extend much beyond 6.4 keV. While the fit with this “PRV+2G+DL” model (model 6 in table 3) is only marginally better than before, the disk line now has a reasonable inclination of $i = 6.5^{+3.8}_{-3.2}$ with an EW of 32 ± 5 eV, and fits the red wing of the line profile well (while the ionized Fe emission models the blue wing: see figure 10c). It is also interesting to note that the centroid energy of the narrow Fe line core increases from 6.368 keV to 6.398 keV (perfectly consistent with 6.400 keV within a 1σ error) in this face-on model ($i \leq 10^\circ$).

The measured width of narrow Fe line core ($\sigma_{\text{obs}} \sim 120$ eV) is much broader than the residual width (σ_{cal}) of a calibration line. Assuming $\sigma_{\text{cal}} = 45$ eV, the intrinsic width of Fe $K\alpha$ line is $\sigma_{\text{int}} = 111^{+11}_{-10}$ eV (or EW of 60 ± 6 eV). This line width is consistent with what was measured with XMM-Newton very recently by Ogle et al. (2005) and Ballantyne et al. (2004). Meanwhile, the additional broad disk line emission provides a better representation of the data if we fixed the center energy at 6.4 keV. Here we have assumed the outer radius of the disk line is $r_{\text{out}} = 1000 r_g$, and a typical steep emissivity of r^{-3} . The inner radius of the disk is constrained to be $r_{\text{in}} = 8.6^{+1.0}_{-0.6} r_g$. A summary of the line parameters is given in table 3.

4.3.2. Line variability

We next consider the iron line variability and its relation to the variation of the baseline continuum component. Due to limited photon statistics, we only traced the variability of the Fe $K\alpha$ line core, using a fixed line width and the centroid energy. For this, a simple power-law plus Gaussian model is adequate to represent the Suzaku data in the 3–10 keV band. Thus, in our approximation, the only parameter that represents the line variability is its normalization (i.e., integrated photon counts in iron line core) measured in different observation epochs. We are aware that this is an oversimplified assumption, given the complicated

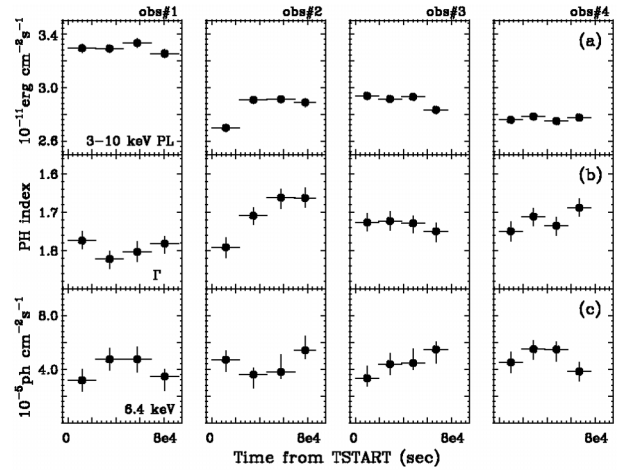


Fig. 11. Spectral variability of baseline power-law component and iron $K\alpha$ core emission. 3–10 keV flux (upper), photon index (middle), and line flux (bottom) are separately shown. 4 XISs data were used for the fitting.

line profile, and that variations with time are even possible for the reflection component. Nevertheless, we believe this is the simplest way of searching for line variability on short timescales. The XIS data were divided into 4 equal time intervals (typically ~ 10 ks) per each #1–#4 observations. Even assuming this simple PL + G model, all of the datasets provide acceptable fits in the statistical sense of $P(\chi^2) \geq 10\%$.

Figure 11 shows the spectral variability of the baseline power-law component and the iron $K\alpha$ core emission. The temporal evolution of the 3–10 keV continuum flux, the photon index, and the Fe line core flux are plotted in the upper, middle, and bottom panels, respectively. Although variability at some level may be present in the light curve of the Fe line core flux, a constant fit provides a good explanation of the data, where $\chi^2/\text{d.o.f} = 17.3/15$ [$P(\chi^2) = 30\%$] and an average iron line photon flux of $F_{\alpha} = (4.41 \pm 0.19) \times 10^{-5}$ ph cm^{-2} s^{-1} . A correlation between the underlying power-law continuum and Fe line fluxes is uncertain, but seems to be absent, as shown in figure 12. These results, however, do not necessarily reject any variations of the iron line profile itself, if the intensity has not changed significantly during the observation. In fact, the iron line profile observed with Suzaku seems to have a somewhat different shape than that observed with the XMM-Newton in 2003. It seems that only the Suzaku data require a strong red-tail, but instead the 6.9 keV emission seems to be a little more “spiky” in the XMM-Newton data (but we need more photon statistics to discriminate this further). A further detailed analysis of the line/absorption features is now on-going and will be presented in a forthcoming paper, especially by a direct comparison of the XMM-Newton and the Suzaku spectra (K. Iwasawa et al. in preparation).

4.4. Excess Soft X-Ray Emission

Finally, we try to model the excess soft X-ray emission below 3 keV, as presented in figure 7. We found that either a steep power-law ($\Gamma = 2.68 \pm 0.04$) or thin thermal

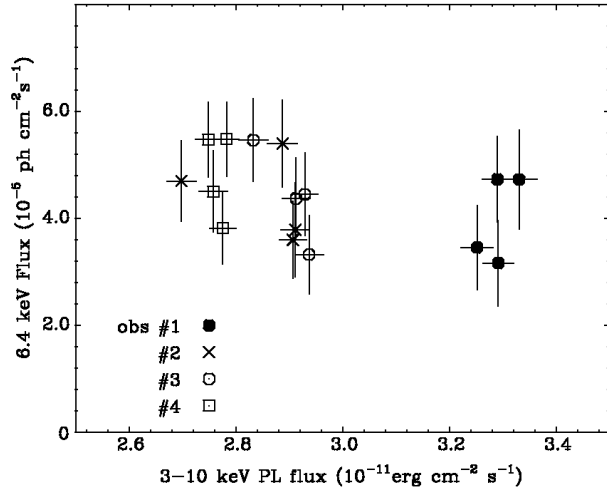


Fig. 12. Comparison of the iron $K\alpha$ core flux versus baseline continuum component. The variability is not clear for the iron line flux.

bremsstrahlung emission ($kT = 1.06 \pm 0.04$ keV) can equally well fit the data with $\chi^2/\text{d.o.f} \simeq 1.1$. Also, the inclusion of an emission line feature near 0.9 keV improves the fit slightly, though it might be an artifact of modeling the XIS data around Ne I K edge (see Ogle et al. 2005 for XMM-Newton RGS soft X-ray spectrum). Interestingly, the excess emission below 3 keV seems a bit *smaller* in this Suzaku spectrum than that reported in the XMM-Newton observation (figure 2 of Ballantyne et al. 2005), for which the source was in a brighter state than any of the Suzaku observations (obs #1–#4). Such excess emission was not necessary in the ASCA analysis (Grandi et al. 1997), but was found in both the ROSAT (Grandi et al. 1997) and BeppoSAX data (Zdziarski & Grandi 2001), as well as in the XMM-Newton data.

This kind of soft excess emission has been observed in other BLRGs (Woźniak et al. 1998) and Sy-1 galaxies, and its nature is currently under debate. For 3C 120, it was first discovered in the Einstein SSS observations (Petre et al. 1984). Grandi et al. (1997) fit the 0.2–2.4 keV ROSAT data and obtained the best fit results with a steep power-law emission of $\Gamma = 2.5$ –3.3, whereas Zdziarski & Grandi favor thin thermal emission of $kT \sim 1$ keV. Very recently, Ogle et al. (2005) suggested a steep power-law with $\Gamma = 2.7 \pm 0.1$, which breaks at 0.6 keV to represent the XMM-Newton data below 1 keV. In contrast, Ballantyne et al. (2004) assumed a thermal bremsstrahlung component in order to reproduce the same X-ray data. Therefore, the situation is not still conclusive, even after the XMM-Newton and the Suzaku observations. However, if the soft excess is due to a collisionally ionized plasma in an extended halo surrounding the nucleus, as suggested in Zdziarski and Grandi (2001), this should vary very little (but see the discussion in Ballantyne et al. 2004).

In fact, in some Seyfert galaxies, the soft excess emission is consistent with being constant, and is likely to be a combination of scattered power-law emission and photoionized gas associated with the AGN Narrow Line Region etc (e.g., Vaughan & Fabian 2004; Reeves et al. 2007). Statistically,

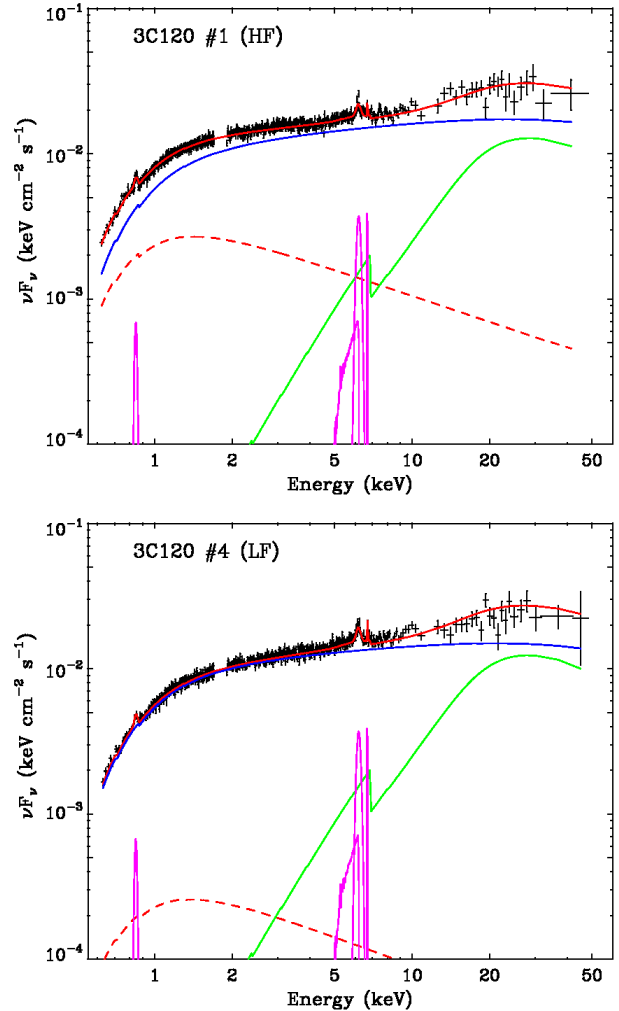


Fig. 13. Broad-band (0.6–50 keV: 3FI-XISs + PIN) spectra of 3C 120 observed with Suzaku in high (upper: obs #1) and low (lower: obs #4) states, with unfolded best-fit model components. Curve through observed points (red): total, curve below the observed points (blue): direct power-law component, curve with a jump in the middle part (green): reflection, discrete lines (purple): iron lines, dashes (red): variable power-law component. The best fit parameters are summarized in table 4.

we cannot rule out there being some thermal/bremsstrahlung emission, but we will discuss below the power-law continuum emission which makes more sense in the context of the two components required to explain the spectral variability (see subsection 4.5). Moreover, with the observed variability being more strongly concentrated at lower energies, a more natural interpretation appears to be a steep power-law component.

4.5. Multiband Spectral Variability

Figure 13 shows the unfolded multiband spectra of 3C 120 obtained with Suzaku in both high (obs #1) and low (obs #4) states. The best-fit model described in the previous sections is taken into account as various emission components in these figures; namely, a direct power-law, Compton reflection, a narrow Fe line core, a 6.9 keV line, a broad disk line, and a steep power-law emission to represent the soft excess

Table 4. Results of spectral fits.*

Component	Parameter	Average	High (obs #1)	Low (obs #4)
wabs	N_{H}^{\dagger}	1.23 [#]	—	—
PRV	Γ	1.74±0.02	1.76±0.03	1.78±0.03
	E_{fold} [keV]	100 [#]	—	—
	R	0.65±0.12	0.79±0.22	0.89±0.20
	i [°]	18.2 [#]	—	—
	$F_{0.6-3 \text{ keV}}^{\ddagger}$	26.2±0.5	28.6±1.5	26.5±1.0
	$F_{3-10 \text{ keV}}^{\ddagger}$	28.7±0.2	30.5±0.5	27.6±0.3
	$F_{10-50 \text{ keV}}^{\ddagger}$	63.3±0.8	68.4±1.5	61.8±1.3
Gauss1	E [keV]	6.40 [#]	—	—
	σ [eV]	111 [#]	—	—
	N_{line}^{\S}	3.14 [#]	—	—
Gauss2	E [keV]	6.93 [#]	—	—
	σ [eV]	10 [#]	—	—
	N_{line}^{\S}	0.69 [#]	—	—
Diskline	E [keV]	6.40 [#]	—	—
	R_{in} [r_{g}]	8.6 [#]	—	—
	i [°]	6.5 [#]	—	—
	N_{line}^{\S}	1.57 [#]	—	—
PL	Γ	2.66±0.04	2.60±0.08	2.65 [#]
	$F_{0.6-3 \text{ keV}}^{\ddagger}$	4.8±0.6	9.3±1.8	1.1 ^{+1.3} _{-1.1}
	$F_{3-10 \text{ keV}}^{\ddagger}$	1.4±0.2	2.9±0.6	0.3 ^{+0.4} _{-0.3}
Gauss3	E [keV]	0.87 [#]	—	—
	σ [eV]	10 [#]	—	—
	N_{line}^{\S}	5.71 [#]	—	—
$\chi^2/\text{d.o.f}$		2978/2768	3018/2884	2853/2729

* The fits to the 0.6–50 keV XIS+PIN time-averaged, co-added spectrum of 3C 120.

[†] Galactic absorption column density in units of 10^{21} cm^{-2} .

[‡] Flux in units of $10^{-12} \text{ erg cm}^{-2} \text{ s}^{-1}$.

[§] Line normalization in units of $10^{-5} \text{ photons cm}^{-2} \text{ s}^{-1}$.

^{||} Assumed to be same as the left, i.e., those assumed to fit an “average” spectrum.

[#] Parameters fixed to these values.

emission below 3 keV. We first assumed the values determined in the previous sections as being initial input parameters, and then re-fit the data again to find a χ^2 minimum under the constraint of fixed iron-line parameters. This is because if we limit the analysis to only above or below 3 keV, as we did in section 4, this avoids having to include a scattered continuum component that could affect the fit. Therefore, we thawed all the parameters, except for the iron-line parameters, to find a “new” χ^2 minimum. The results of the fits are summarized in table 4 for various cases: (1) time-averaged spectra (obs #1–#4 summed), (2) high flux state (HF, obs #1), and (3) low flux state (LF, obs #4), respectively. A direct comparison of the multiband spectra between the HF and LF states (figure 14) clearly indicates an energy dependence of the spectral evolution in different states of the source activity.

Thus, it is interesting to consider what spectral component is primarily responsible for the spectral variability in 3C 120. As can be seen in table 4 and figure 13,

the underlying continuum emission (i.e., the sum of the direct power-law plus reflection) varies only slightly. In fact, the spectral shapes, as measured by a photon index of $\Gamma \simeq 1.75$ in LF and HF states, are consistent within the statistical error. The flux actually changes between the LF and HF states, but only at the 10% level between 0.6–50 keV. In contrast, a factor of ≥ 5 variability has been observed for the steep power-law component where the 0.6–3 keV flux changes significantly from $(9.3 \pm 1.8) \times 10^{-12} \text{ erg cm}^{-2} \text{ s}^{-1}$ to $(1.1^{+1.3}_{-1.1}) \times 10^{-12} \text{ erg cm}^{-2} \text{ s}^{-1}$. Actually, this steep power-law component is not visible when the source is in a low flux state, and only appears when the source is in a brighter state. This is consistent with the fact that the XMM-Newton spectrum showed a slightly larger amount of soft excess emission when the source was in a relatively bright flux state compared to any of the Suzaku observations described in this paper.

To further examine the origin of the spectral variability, the difference spectrum of the HF minus LF spectra was

Table 5. Results of spectral fits to the 0.3–50 keV *difference* spectrum between obs #1 and obs #4.

Model*	kT [keV]	F_{brm}^{\dagger}	Γ_1^{\ddagger}	F_{PL1}^{\dagger}	Γ_2^{\ddagger}	F_{PL2}^{\dagger}	$\chi^2/\text{d.o.f}$
wabs + Bremsung	2.53 ± 0.07	13.0 ± 0.5	453/192
wabs + PL	2.22 ± 0.02	14.8 ± 0.2	198/192
wabs + 2PL	2.65^{\parallel}	9.4 ± 0.3	1.75^{\parallel}	6.3 ± 0.3	198/192

* A thin-thermal or power-law function modified by Galactic absorption of $N_{\text{H}} = 1.23 \times 10^{23} \text{ cm}^2$.

\dagger 0.6–10 keV flux in units of $10^{-12} \text{ erg cm}^{-2} \text{ s}^{-1}$.

\ddagger Differential spectral photon index.

\parallel Parameters fixed to these values.

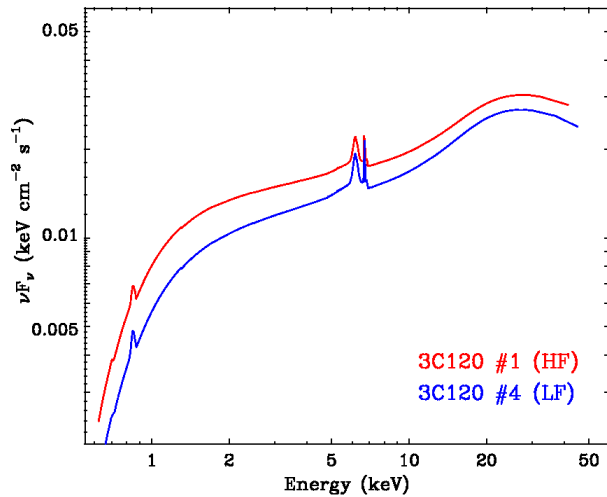


Fig. 14. Comparison of the best-fit broad-band (0.6–50 keV) model of 3C 120 observed with Suzaku in high flux (HF; upper red: obs #1) and low flux (LF; lower blue: obs #4) states with the best-fit model functions. The best fit parameters for HF/LF states are summarized in table 4.

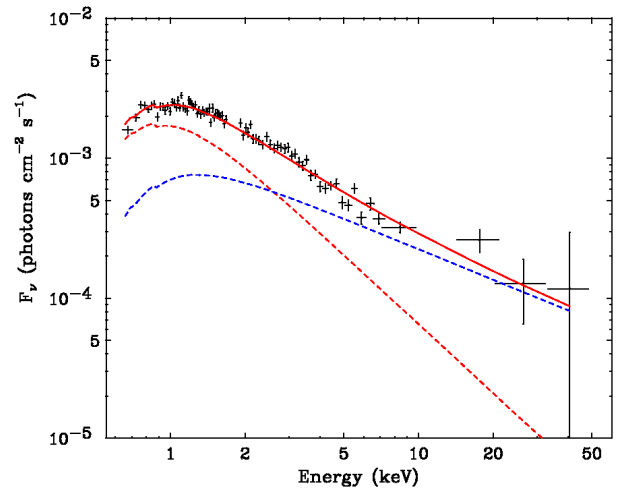


Fig. 15. Difference spectrum of 3C 120 between the high (obs #1) and low (obs #4) flux states in the Suzaku observation (3 FI-XISs + PIN). Although the difference spectrum is well represented by an absorbed power-law of $\Gamma = 2.22 \pm 0.02$ in the XIS energy band, some residuals remain above 10 keV. The overall spectrum (including HXD/PIN) is better represented by a double power-law function, where the low energy emission (below 3 keV) is dominated by a steep power-law of $\Gamma = 2.65$ (red dashes) and the high energy emission (above 10 keV) is modified by a flat power-law of $\Gamma = 1.75$ (blue dashes).

extracted, using both the XIS and HXD/PIN data. The difference spectrum is plotted in figure 15. This technique clearly shows the variable component of the emission from 3C 120 modified by absorption, with the constant components in the spectrum being subtracted. The resulting difference spectrum was fitted very well with a simple power-law of photon index $\Gamma = 2.22 \pm 0.02$ and fixed $N_{\text{H}} = 1.23 \times 10^{21} \text{ cm}^{-2}$, with fit statistics of $\chi^2/\text{d.o.f} = 198/192$. Note that the inclusion of a thin thermal emission component provides a rather poor fit, as shown in table 5.

Although this spectral shape is a bit flatter than a steep power-law describing the soft excess emission ($\Gamma \simeq 2.7$; see PL of table 4), only small variations in the underlying continuum emission (PRV: $\Gamma \simeq 1.7$) can easily account for this apparent discrepancy. In fact, the same difference spectrum can be equally well fitted with double power-law functions, where the low-energy emission is dominated by a steep power-law ($\Gamma_1 = 2.65$, which mimics the soft “variable” power-law) and the high energy emission is represented by a flat power-law ($\Gamma_2 = 1.75$, which mimics the hard “direct” power-law component). These model components are presented in

figure 15 as red and blue dashes, respectively.

We also note that a normalization of the HXD/PIN difference spectrum seems to be slightly larger than an extrapolation of the XIS spectrum above 10 keV. This may imply both intrinsic and reprocessed component changes together in 3C 120, though it was not the case for MCG –6–30–15, where the reflected component was constant and only the intrinsic power-law varied (Miniutti et al. 2007: see also subsection 5.3). However, we suspect a part of the reason could be instrumental: As we showed in section 2 and in Appendix, the current background models of the HXD/PIN would produce $\sim 5\%$ systematics in the background subtraction, which corresponds to $\sim 20\%$ uncertainties in the 3C 120 flux above 10 keV. This could be more enhanced in the difference spectrum, as shown in figure 15. We will discuss more about this in a forthcoming paper using update background models of the HXD/PIN.

5. Discussion

5.1. *Suzaku* View of 3C 120

In previous sections, we presented temporal and spectral analysis of a *Suzaku* observation of 3C 120 in 2006 February and March. The great advantage of *Suzaku* is that both the XIS and HXD/PIN have excellent sensitivity, so that we can resolve the spectral evolution of this source over two decades in frequency, even within a short (40ks) exposure. During the *Suzaku* observations, 3C 120 was in a relatively low flux state of $F_{2-10\text{ keV}} = 3.9 \times 10^{-11} \text{ erg cm}^{-2} \text{ s}^{-1}$ on average, though the flux decreased gradually from $4.4 \times 10^{-11} \text{ erg cm}^{-2} \text{ s}^{-1}$ to $3.6 \times 10^{-11} \text{ erg cm}^{-2} \text{ s}^{-1}$ between obs #1 and obs #4. Historically, the maximum flux observed by *Suzaku* (that obtained in obs #1) is almost consistent with what was observed by ASCA in 1994, by Beppo-SAX in 1997 and by XMM-Newton in 2003 ($F_{2-10\text{ keV}} \sim 4.6 \times 10^{-11} \text{ erg cm}^{-2} \text{ s}^{-1}$; Reynolds 1997; Zdziarski & Grandi 2001; Ballantyne et al. 2004), but 40% lower than that reported by RXTE in 1998 (Eracleous et al. 2000). This range of variability is natural considering the long-term variability of this source over year-long timescales in X-rays (Marscher et al. 2002; Markowitz & Edelson 2004).

Using the high-sensitivity, broad-band instruments onboard *Suzaku*, we confirmed various important characteristics of 3C 120: (1) the presence of a relatively narrow ($\sigma = 111_{-10}^{+11} \text{ eV}$ or EW of $60 \pm 6 \text{ eV}$) Fe line core centered at 6.4 keV (see Ballantyne et al. 2004; Ogle et al. 2005 for XMM-Newton analysis). In addition, *Suzaku* has unambiguously confirmed the broad iron line component, which may be possibly related to an extremely broad line feature observed with ASCA (Grandi et al. 1997; Reynolds 1997; Sambruna et al. 1999); (2) a relatively weak reflection component ($R = 0.65 \pm 0.12$: see table 4), determined with much better accuracy than that observed with Beppo-SAX ($R = 0.56_{-0.20}^{+0.44}$: Zdziarski & Grandi 2001) and RXTE ($R = 0.4_{-0.1}^{+0.4}$: Eracleous et al. 2000; see also Ballantyne et al. 2004 for updated results) under the same constrained parameters; (3) the presence of a soft excess emission component below 3 keV, as first reported by Einstein (Turner et al. 1991) and by ROSAT (Grandi et al. 1997). Finally, we confirmed the spectral variability of 3C 120, whereby the spectra becomes softer when it becomes brighter, as suggested by Maraschi et al. (1991) and Zdziarski and Grandi (2001).

The important question possibly raised by readers is “what is completely NEW for *Suzaku*?” First of all, we discovered, for the first time, the presence of a broad red-tail (asymmetric red wing) in the Fe $K\alpha$ line of any radio galaxy. Interestingly, the line profile of 3C 120 is quite similar to those found in some Seyfert galaxies (e.g., MCG –5–23–16; Reeves et al. 2007), which provides important challenges to the unification models of radio-loud/quiet AGNs. We also detected a 6.9 keV line, but perhaps not as clearly as first noticed in the XMM-Newton data in 2003 (Ballantyne et al. 2004). This may suggest significant changes in the Fe line profile on the year-long timescale, but further deep/long monitoring of 3C 120 is necessary for this kind of study. Also, we have shown that *Suzaku* can provide a new diagnosis for accurately measuring the line center energy (subsection 4.3), which was not possible before.

Second, we found that the excess variance (i.e., variability amplitude) is generally larger at lower energies. From detailed multiband spectral studies, we conclude the primary “variable” component is a steep ($\Gamma = 2.6 - 2.7$) power-law, which, at the same time, accounts for the soft excess emission below 3 keV. In fact, the difference spectrum is well represented by a steep power-law ($\Gamma_1 = 2.65$) modified by a flatter second component ($\Gamma_2 = 1.75$) at higher energies. Apparently, the flat component mimics the “direct” power-law emission from the 3C 120 nucleus, and varied only a little (10%) during our observations. In contrast the flux of the steep power-law emission may have changed by a factor of ≥ 5 in the transition between the HF and LF states. Below we discuss these new findings provided by *Suzaku* and their interpretation in detail.

5.2. *Nature of the Iron K Line Complex*

Suzaku successfully resolved the iron K line complex of 3C 120, and was also first to verify the broad component’s asymmetry. We showed that the iron line complex is composed of (1) a relatively narrow, neutral iron K line core, (2) broad iron line emission possibly emitted from the accretion disk (see subsection 4.3), and (3) an ionized $\sim 6.9 \text{ keV}$ line. Interestingly, any of the models assuming a simple Gaussian profile (model 2, 4, 5 in table 3) and/or an “edge-on” disk (model 5) predicts that the centroid energy of the narrow line core is slightly shifted redwards by $\sim 30 \text{ eV}$. Meanwhile, the energy of the narrow core increases from 6.368 keV to 6.398 keV in the face-on model (model 6), which is then formally consistent with neutral iron at 6.40 keV. We suspect this is because the face-on diskline contributes towards some of the flux of the narrow 6.4 keV line core. For instance, the observed 30 eV shift of the line core implies a typical radius of $\sim 200 r_g$ if the red-shift is purely gravitational.

In contrast, the intrinsic line width of the narrow Fe line core was measured to be $\sigma \simeq 110 \text{ eV}$. Assuming that this line width is simply caused by Doppler broadening, this corresponds to a FWHM velocity of 10^4 km s^{-1} , indicating a possible origin in the broad line region (BLR). In the optical region, the FWHM velocity of the BLR, as measured by Peterson et al. (2004) using the $H\beta$ is smaller, $2200 \pm 200 \text{ km s}^{-1}$. Alternatively, Ogle et al. (2005) provides a very high S/N optical spectrum which shows a broader ($\gg 2000 \text{ km s}^{-1}$) component associated with the BLR lines. This would be then more consistent with the width of the Fe line core if that also originates from the BLR. Thus, we suggest that most of the flux of the narrow 6.4 keV line core could be from the BLR, but that the outer disk ($\sim 200 r_g$) also makes some contribution.

The residuals present after subtracting the iron line core (figure 10b) are poorly modeled either by adding a simple broad Gaussian or by adding the Compton shoulder of the $K\alpha$ line, as discussed in subsection 4.3. One may also suggest whether the presence of a warm absorber may affect the continuum curvature to make an apparent red-tail below the iron K line. In this context, Ogle et al. (2005) presented a very high S/N RGS spectrum, and there do not appear to be any significant lines or edges due to a warm absorber. Thus, the warm absorber must be very weak, or even absent, in 3C 120 (but not surprising if we are viewing face-on). This also

means that it is rather unlikely that any additional absorption can effect the Fe K line modeling, especially the red-wing (see also subsection 4.5). Rather, a significant red-tail below 6.4 keV (in the rest frame of source) favors diskline emission from the inner accretion disk of $r_{\text{in}} \simeq 8.6_{-0.6}^{+1.0} r_g$. Indeed, adding the diskline emission provides a much better fit statistic than any other model, as summarized in table 3. If this broad line really originates from the inner accretion disk, it should provide important clues regarding jet formation in the accretion disk.

For example, Reeves et al. (2007) discovered a similar broad iron line in the Suzaku/XMM-Newton spectra of MCG –5–23–16, which is thought to originate from the inner accretion disk ($r_{\text{in}} \simeq 20 r_g$). These observations may imply that both the radio-loud 3C 120 and the radio-quiet MCG –5–23–16 have similar accretion disk structures, in contrast to suggestions that the optically-thick accretion disk is truncated in 3C 120 to a hot, optically thin flow at a distance of $r_{\text{in}} \sim 100 r_g$ (Eracleous et al. 2000; Zdziarki & Grandi 2001; Ballantyne et al. 2004). We also note that an EW of the diskline is 32 ± 5 eV, whereas that for the narrow Fe line core is 60 ± 6 eV. Given the prediction of George and Fabian (1991) that a reflection parameter, R , should be equal to $EW(\text{eV})/150(\text{eV})$, the iron line EW is expected to be 90 eV for the level of Compton reflection $R \simeq 0.6$. Interestingly, this is consistent with the sum of the EW s of the narrow and diskline components, and therefore the Compton hump could possibly be associated with both lines. Observations of the iron line profiles in various other broad-line radio galaxies are important for the systematic comparison between Seyferts and BLRGs. We are planning to submit further deep observations of other BLRGs in the next Suzaku observation program to test this idea.

Finally, to further test the robustness of the iron K disk line, we tried an alternative partial covering model, to see if that can reproduce the broad residuals present in the iron K band. Instead of the broad line, the neutral partial covering XSPEC model PCFABS was included, and the XIS+HXD data re-fitted over the range from 0.6–50 keV. The model assumes an absorbed double power-law continuum, together with a single Gaussian line to model the iron $K\alpha$ line core, and ionized iron K emission, as described previously, while Compton reflection is also included in the model with a cut-off energy of 100 keV. The partial covering model results in a fit statistic of 2999/2769, and leaves significant residuals around 6 keV in the iron K band. The fit statistic is statistically worse than the diskline fit ($\Delta\chi^2 = 21$ for 1 extra parameter), while the disk line has fit statistic of 2978/2768 (see subsection 4.5), and the equivalent width of the diskline is 45 eV. Without including either a diskline or a partial coverer, the fit statistic is 3018/2771. For a 50% covering fraction, the upper-limit on the column density is then $< 3 \times 10^{21} \text{ cm}^{-2}$. Therefore, the detection of the broad iron line appears to be robust in 3C 120.

5.3. “Hidden” Jet Emission?

In subsection 4.5, we considered the origin of the spectral variability in 3C 120 by comparing the multiband spectra obtained in low flux (LF) and high flux (HF) states. Interestingly, several authors have examined similar spectral

evolution of radio-quiet Seyfert galaxies. For example, Miniutti et al. (2007) compared multiband spectra of the Sy-1 MCG –6–30–15 obtained in the LF and HF states. They found that difference spectrum shows a steep power-law of $\Gamma = 2.2$, which is consistent with the direct power-law emission observed in both the LF and HF states (also see figure 16). This leads to an idea that the broad band spectral variability of MCG –6–30–15 is decomposed into two components: a highly variable power-law (direct nucleus emission) and a constant reflection component plus iron line emission. Similarly, Reeves et al. (2007) presented a difference spectrum of a Sy-2 galaxy, MCG –5–23–16, which was fitted extremely well by a simple absorbed power-law of $\Gamma = 1.9$. Again, this spectral shape is exactly consistent with the direct power-law component, which they observed in LF and HF states. Furthermore, there are no residuals present in the iron K band or any excess counts in the HXD/PIN difference spectrum above 10 keV.

In contrast to these findings for Seyfert galaxies, an interesting discovery made by Suzaku is that the variable component in 3C 120 is much steeper ($\Gamma \simeq 2.7$) than the power-law emission reported in literature ($1.6 \leq \Gamma \leq 1.8$: see also Marscher et al. 2002). One interesting idea to account for this steep, variable emission is the beamed radiation from the jet [not on kpc scales as discussed in Harris et al. (2004) and section 1, but the unresolved base of the jet on sub-pc scales), though this component contributes only $\sim 20\%$, at most, of the Sy-1 like X-ray emission in 3C 120 (i.e., emitted from the disk and corona). In fact, 3C 120 possesses a superluminal radio jet with an inclination angle $\leq 14^\circ$ (Eracleous & Halpern 1988). This low inclination angle implies that 3C 120 may have some “blazar-like” characteristics, such as rapid X-ray variability or a non-thermal spectrum extending to the γ -ray energy band. For example, if we assume a jet bulk Lorentz factor of $\Gamma_{\text{BLK}} = 10$ and a jet inclination angle of 14° , we can expect the observed flux to be mildly “boosted” towards the observer with a Doppler beaming factor $\delta \sim 3$. Also note that the X-ray spectra of blazars are generally represented by a power-law function, but their X-ray photon indices range widely ($1.5 \leq \Gamma \leq 3.0$: Kubo et al. 1998) among various sub-classes (e.g., HBL, LBL, and FSRQ: e.g., Fossati et al. 1998). Interestingly, similarly variable, steep power-law emission has been found for a distant ($z = 0.94$) quasar, PG 1407+265, which is classified as a radio-quiet object, but shows strong evidence of a radio jet with a highly relativistic speed in VLBA observations (Gallo 2006).

Figure 16 shows the multi-band spectrum of 3C 120 (upper), compared to that of the radio-quiet Sy-1 galaxy MCG –6–30–15 (lower) between the radio and X-ray energy bands. Note the significant difference in the radio band (as inferred by a definition of radio-quiet/loud objects), but spectral similarity in the optical band. In both figures, the X-ray data come from recent Suzaku observations. Two lines around 10^{18} Hz show the best-fit X-ray spectral model during HF/LF states. The difference spectrum is shown as a thick dashed line. The origin of the variable component (steep power-law) in 3C 120 is still uncertain, but here we assume the non-thermal jet dominates this power-law emission. The thin dotted line shows an example fit with a one-zone homogeneous SSC (synchrotron

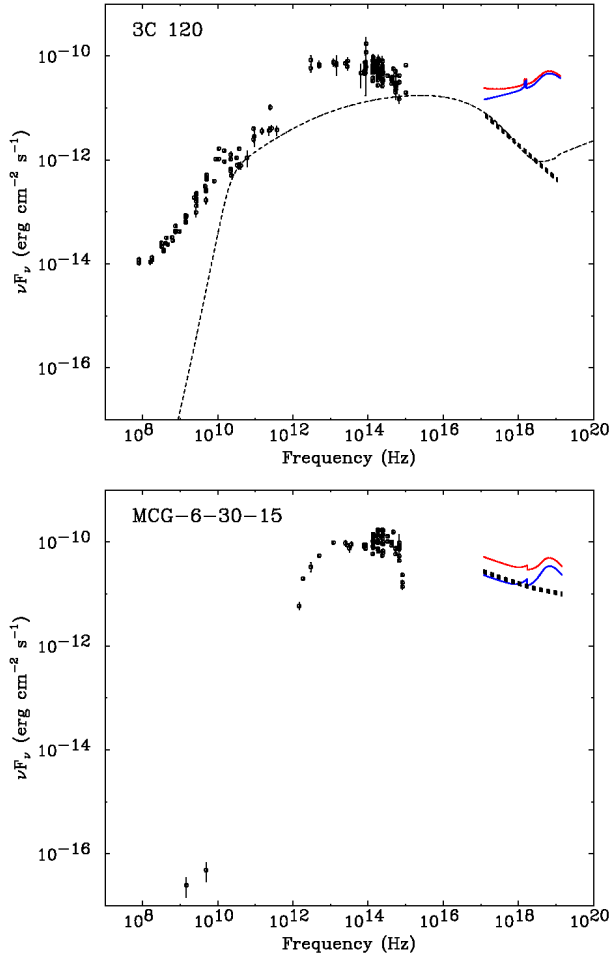


Fig. 16. Comparison of the multiband spectrum of a radio-loud BLRG 3C 120 (upper) and a radio-quiet Sy-1 galaxy MCG -6-30-15 (lower). In both figures, X-ray data come from the most recent Suzaku observations (3C 120: this work; MCG -6-30-15: Miniutti et al. 2007) and the other data comes from the NED data base. In two curves at around 10^{18} Hz, upper side line (red) shows the best-fit X-ray spectral model during the high state, whereas lower side line (blue) shows that for the low state. The variable power-law component is shown as a thick dashed line for 3C 120, whereas the difference spectrum is shown for MCG -6-30-15. The thin dotted line corresponds to an example fit of the one-zone homogeneous SSC model, as described in the text.

self-Compton) model described in Kataoka et al. (1999), where the soft X-ray excess corresponds to the highest energy end of the synchrotron emission.

Also, above 10 keV, the inverse Compton component is possibly present even in the hard X-ray band, but the isotropic Seyfert-like emission overwhelms that blazar-like emission, where the relativistic boost of the jet is smaller than in blazars, because of a lower δ . Note that this model for the jet-like emission — with the SED peaking at $\sim 3 \times 10^{15}$ – 10^{16} Hz — implies HBL-like classification of the jetted emission. This in principle fits well with the FR-I type classification of the object discussed in section 1, where HBL blazars are FR-I radio galaxies viewed close to the direction of the jet. However, there is an additional complication: the FR-I/HBL nature of this object as inferred from the

radio observations and the soft X-ray excess is in conflict with the presence of broad emission lines, present in the optical spectrum, since those are generally not observed in FR-I sources.

Interestingly, the jet parameters derived here are consistent with typical values for blazars, except for a moderate beaming factor of $\delta = 3$ (viz $5 \leq \delta \leq 30$ for blazars; e.g., Kubo et al. 1998): magnetic field $B = 0.3$ G, region size $R = ct_{\text{var}} \delta \sim 1.0 \times 10^{17}$ cm, under an assumption of equipartition between electron and field energy densities ($u_e = u_B$). We assumed a broken power-law form of the electron distribution $N(\gamma) \propto \gamma^{-s} (1 + \gamma/\gamma_{\text{br}})^{-1} \exp(-\gamma/\gamma_{\text{max}})$, where γ is the electron energy (in units of $m_e c^2$), $\gamma_{\text{brk}} = 10^3$, $\gamma_{\text{max}} = 1.3 \times 10^5$, and $s = 1.8$. Surprisingly, this simple jet model reproduces the general trend of the spectral energy distribution quite well, though some discrepancies are seen in the radio band. Such discrepancies in the radio are found in many studies, and it is believed to be a consequence of the radio emission originating from a much larger region than the X-rays (e.g., Kataoka et al. 1999). Also note that the prediction of gamma-ray flux via inverse Comptonization is less than 10^{-10} erg cm $^{-2}$ s $^{-1}$, qualitatively consistent with the non-detection by EGRET and COMPTEL onboard CGRO.

Based on these facts alone, it is still premature to conclude that the steep variable X-ray emission is actually originating from the jet in 3C 120. Maraschi et al. (1991) and Zdziarski & Grandi (2001) claimed that an X-ray jet component could, at the very least, dilute the Seyfert-like spectrum of 3C 120, and may account for the observed weak reflection features. This idea is straightforward, but may be oversimplified by following reasons: (1) the Suzaku observations have now revealed that the variable emission can explain at most 20% of the Sy-1 emission even below 3 keV. (2) The putative jet spectrum is much steeper than the direct power-law ($\Gamma \simeq 1.7$). Such a low-amplitude, steep power-law jet component cannot dilute the Sy-1 emission sufficiently, especially above 5 keV (where the iron lines and reflection become important, unless there is additional, weak contribution from a hard spectrum due to the inverse Compton component.⁴) (3) No evidence for “blazar-like” variability has been found above 2 keV (Gliozzi et al. 2003; Marshall et al. 2003). Therefore, it seems that the weak iron line and the reflection hump observed in BLRGs (Eracleous et al. 2000) might be more intrinsic, and provide important clues to the origin of the jet-like emission.

Nevertheless, we showed that the variable steep X-ray emission is a key to understanding the spectral evolution of 3C 120. In particular, it seems that the steep power-law component is more significant when the source is brighter, and can well explain the significant soft excess repeatedly observed in the literature for this AGN. Interestingly, the soft excess emission is hardly visible when the source becomes fainter, which may indicate that the jet component has completely disappeared and/or is hidden behind much stronger Sy-1 emission.

⁴ In this context, we note that an inverse Compton model in figure 16 is dependent on input parameters as $f_{\text{IC}} \propto u_B^{-2}$, where f_{IC} is an observed inverse Compton flux. Therefore this could dilute the Sy-1 emission only if the magnetic field strength is about a factor of five smaller than equipartition values, which is often not the case for blazars (see, e.g., Kubo et al. 1998).

Unfortunately, the flux changes of 3C 120 during the Suzaku observation were relatively small, so we cannot conclude what fraction of the X-ray flux is actually explained by the jet. Future deep Suzaku observations, as well as continuing VLBI monitoring coincident with X-ray monitoring (as the campaigns reported by Marscher et al. 2002), sensitive measurements with GLAST, in quite different states of source activity (i.e., observations at historically high and low states) will be crucial to understanding the nature of the emission properties in 3C 120 (see recent paper by Grandi & Palumbo 2007) for the detectability with GLAST at MeV–GeV energy band).

6. Conclusion

We have presented a detailed analysis of results from the broad line radio galaxy 3C 120 observed with Suzaku from 2006 February and March. Thanks to the excellent sensitivity of both the XIS and HXD/PIN detectors onboard Suzaku, we obtained multi-band data with unprecedented accuracy between 0.6 and 50 keV. Our major findings are as follows:

- (1) The overall spectral shape, including weak reflection ($R \simeq 0.6$) and a soft excess, which was consistent with previous findings, and was determined with unprecedented accuracy.
- (2) We confirmed the presence of a narrow iron $K\alpha$ core with a width of $\sigma = 111_{-10}^{+11}$ eV (and an $EW = 60 \pm 6$ eV), and a 6.93 ± 0.02 keV emission line, possibly emitted from H-like iron.
- (3) After subtracting these narrow line components, significant residuals remained redwards of the narrow iron line core, well below 6.4 keV.
- (4) The difference spectrum between LF and HF clearly shows a power-law of $\Gamma = 2.2$, which is naturally interpreted as being the combination of a highly variable steep power-law ($\Gamma = 2.7$; jet-like) plus a moderately variable direct power-law emission ($\Gamma = 1.7$; Sy-1 like). No significant variability was found in either the Fe K line emission or reflection component.

We argue that the narrow iron K line is primarily emitted from the broad line region corresponding to a FWHM velocity of 10^4 km s^{-1} , but the emission from the outer disk ($\sim 200 r_g$) may also play a part. Meanwhile, the broad redshifted iron line can be interpreted as being emission from the inner, face-on accretion disk ($r_{in} \sim 10 r_g$ and $i \leq 10^\circ$). We considered the origin of a highly variable steep power-law component in the context of a possible relation to non-thermal jet emission. Although we cannot conclude what fraction of X-ray emission in 3C 120 is actually explained by the jet, it must be less than 20% of the ‘‘Sy-1 like’’ emission even below 3 keV. This clear difference in the spectral evolution between Sy-1s and 3C 120 provides an important motivation for further future deep observations of BLRGs.

Finally, we thank an anonymous referee for his/her constructive comments, which helped us to clarify many of the issues presented in this paper. We also thank Dr. Tahir Yaqoob for his helpful comments and discussion on the Suzaku data analysis.

Appendix. Effect of Background Variations on the HXD/PIN Light Curve

Here we provide a follow-up discussion concerning the robustness of background subtraction of the HXD/PIN using the most recent response and background model as of 2006 November (v1.2 data and `ae_hxd_pininom_20060814.rsp`). Detailed studies of the background systematics are still under investigation by the HXD instrumental team, but a careful comparison of the HXD/PIN light curves (see figure 3) with the background variations may provide important hints for future modeling of relatively faint sources. For this aim, 3C 120 is a good target, because it is bright enough to be firmly detected by the HXD/PIN, but much fainter than the background photon statistic. As we have seen in figure 2, the net intensity of 3C 120 is expected to be $\sim 30\%$ of the non-X-ray background plus CXB above 12 keV.

Figure 17 compares the temporal variations of the total HXD/PIN counts (upper blue: including source and background), the non-X-ray background model A (middle green; see subsection 2.2), and resultant estimate of source counts from 3C 120 (lower red). The HXD/PIN count rate (blue) is highly variable from 0.5 cts s^{-1} to 0.9 cts s^{-1} , and this trend is generally well reproduced in the background model (green). The dead time is corrected for each of the time bins, because it varies with the event rate (dominated by background photons) of the HXD/PIN detector and ranges from 3.5% to 8.5% during 3C 120 #1–#4 observations. As a result, small residuals (of 5–10% background level) remains after subtracting the background photons, especially when the total HXD/PIN counts exceeds ~ 0.7 cts s^{-1} . Since these time regions correspond to orbits where the COR is low and/or passing through the SAA, a long-decay component of the background may have not been modeled perfectly in the current data.

Similarly, the relative lack of variability in the XIS light curve suggests apparent ‘‘rapid’’ changes in HXD/PIN flux figure 17 could be artifacts of the background subtraction. Nevertheless, the general trend of the HXD/PIN flux variations traces well those of the XIS data below 10 keV, as we have seen in figure 5. The average net source count rate of the HXD/PIN is 0.195 ± 0.005 cts s^{-1} , 0.177 ± 0.005 cts s^{-1} , 0.180 ± 0.004 cts s^{-1} , and 0.165 ± 0.004 cts s^{-1} respectively, and hence the maximum is in obs #1 and the minimum in #4, as per the XIS. A constant fit to the overall HXD/PIN light curves (obs #1–#4) provides $\chi^2/\text{d.o.f} = 154/80$. Even after removing the time regions where the background is high (HXD/PIN counts exceeds 0.7 cts s^{-1}), we obtained $\chi^2/\text{d.o.f} = 103/71$ [$P(\chi^2) = 0.7\%$]. Therefore, we think the long-term variations of 3C 120 are robust in the 12–40 keV energy band. A more detailed discussion using revised background models will be presented elsewhere.

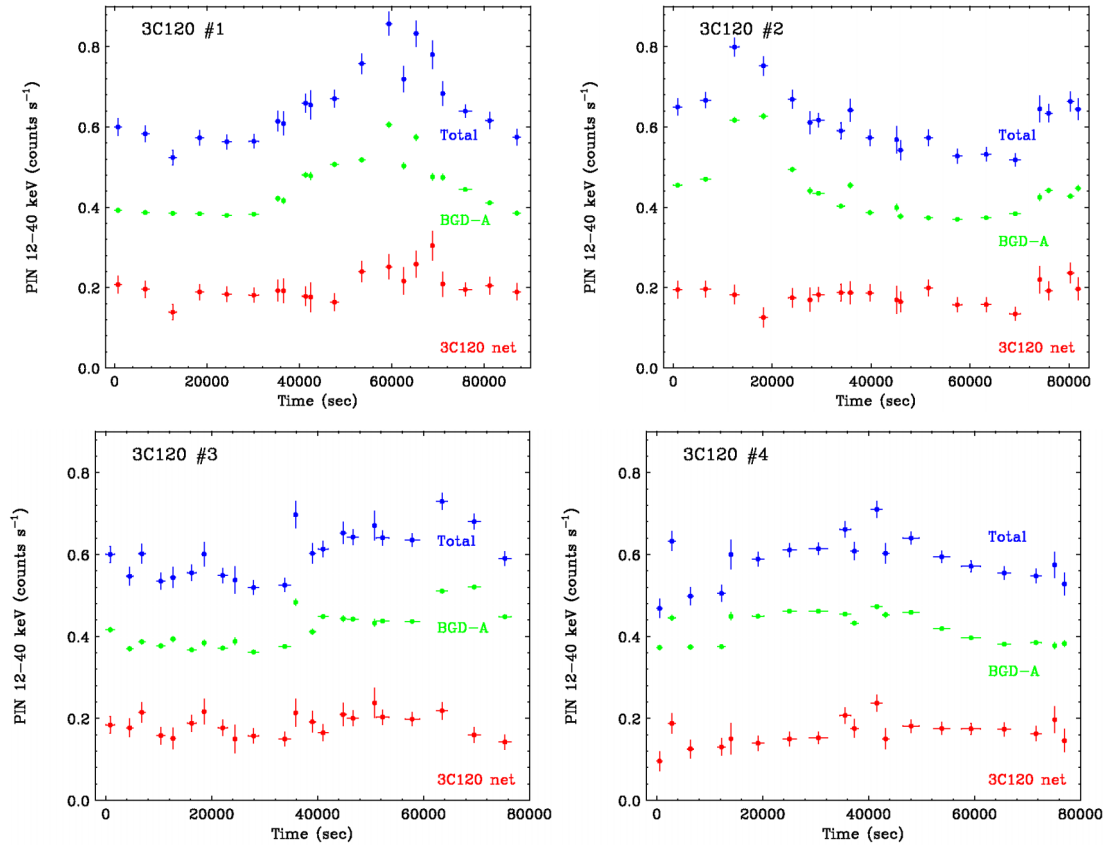


Fig. 17. Comparison of the temporal variation of total HXD/PIN counts (upper blue: including source and background), non-X-ray background model A (middle green; see subsection 2.2), and resultant estimate of the source counts from 3C 120 (lower red) for 3C 120 #1–#4.

References

- Ballantyne, D. R., Fabian, A. C., & Iwasawa, K. 2004, *MNRAS*, 354, 839
- Baum, S. A., Zirbel, E. L., & O’Dea, C. P. 1995, *ApJ*, 451, 88
- Elvis, M., Wilkes, B. J., & Lockman, F. J. 1989, *AJ*, 97, 777
- Eracleous, M., & Halpern, J. P. 1998, *ApJ*, 505, 577
- Eracleous, M., Sambruna, R., & Mushotzky, R. F. 2000, *ApJ*, 537, 654
- Fabian, A. C., et al. 2002, *MNRAS*, 335, L1
- Fabian, A. C., Rees, M. J., Stella, L., & White, N. E. 1989, *MNRAS*, 238, 729
- Fossati, G., Maraschi, L., Celotti, A., Comastri, A., & Ghisellini, G. 1998, *ApJ*, *MNRAS*, 299, 433
- Fujimoto, R., et al. 2007, *PASJ*, 59, S133
- Fukazawa, Y., et al. 2006, *Proc. SPIE*, 6266, 75
- Gallo, L. C. 2006, *MNRAS*, 365, 960
- George, I. M., & Fabian, A. C. 1991, *MNRAS*, 249, 352
- Gliozzi, M., Sambruna, R. M., & Eracleous, M. 2003, *ApJ*, 584, 176
- Grandi, P., & Palumbo, G. G. C. 2007, *ApJ* in press (astro-ph/0611342)
- Grandi, P., Sambruna, R. M., Maraschi, L., Matt, G., Urry, C. M., & Mushotzky, R. F. 1997, *ApJ*, 487, 636
- Gruber, D. E., Matteson, J. L., Peterson, L. E., & Jung, G. V. 1999, *ApJ*, 520, 124
- Haardt, F., & Maraschi, L. 1991, *ApJ*, 380, L51
- Harris, D. E., Mossman, A. E., & Walker, R. C. 2004, *ApJ*, 615, 161
- Iwasawa, K., et al. 1996, *MNRAS*, 282, 1038
- Iwasawa, K., Fabian, A. C., Young, A. J., Inoue, H., & Matsumoto, C. 1999, *MNRAS*, 306, L19
- Iwasawa, K., Miniutti, G., & Fabian, A. C. 2004, *MNRAS*, 355, 1073
- Junor, W., Biretta, J. A., & Libio, M. 1999, *Nature*, 401, 891
- Kataoka, J., et al. 1999, *ApJ*, 514, 138
- Kellermann, K. I., Sramek, R., Schmidt, M., Shaffer, D. B., & Green, R. 1989, *AJ*, 98, 1195
- Kokubun, M., et al. 2007, *PASJ*, 59, S53
- Koyama, K., et al. 2007, *PASJ*, 59, S23
- Kubo, H., Takahashi, T., Madejski, G., Tashiro, M., Makino, F., Inoue, S., & Takahara, F. 1998, *ApJ*, 504, 693
- Livio, M. 1999, *Phys. Rep.* 311, 225
- Magdziarz, P., & Zdziarski, A. 1995, *MNRAS*, 273, 837
- Maraschi, L., Chiappetti, L., Falomo, R., Garilli, B., Malkan, M., Tagliaferri, G., Tanzi, E. G., & Treves, A. 1991, *ApJ*, 368, 138
- Markowitz, A., & Edelson, R. 2004, *ApJ*, 617, 939
- Marscher, A. P., et al. 2002, *Nature*, 417, 625
- Marshall, K., Ferrara, E. C., Miller, H. R., Marscher, A. P., & Madejski, G. 2004, in *Proc. X-ray Timing 2003: Rossi and Beyond*, ed. P. Kaaret, F. K. Lamb, & J. H. Swank (Melville, NY: AIP), 182
- Matt, G. 2002, *MNRAS*, 337, 147
- Miniutti, G., et al. 2007, *PASJ*, 59, S315
- Mitsuda, K., et al. 2007, *PASJ*, 59, S1
- Moles, M., del Olmo, A., Masegosa, J., & Perea, J. D. 1988, *A&A*, 197, 1

- Nandra, K., George, I. M., Mushotzky, R. F., Turner, T. J., & Yaqoob, T. 1997, *ApJ*, 477, 602
- Nandra, K., George, I. M., Mushotzky, R. F., Turner, T. J., & Yaqoob, T. 1999, *ApJ*, 523, L17
- Ogle, P. M., Davis, S. W., Antonucci, R. R. J., Colbert, J. W., Malkan, M. A., Page, M. J., Sasseen, T. P., & Tornikoski, M. 2005, *ApJ*, 618, 139
- Page, M. J., et al. 2001. *A&A*, 365, L152
- Peterson, B. M., et al. 2004. *ApJ*, 613, 682
- Petre, R., Mushotzky, R. F., Holt, S. S., & Krolik, J. H. 1984, *ApJ*, 280, 499
- Poutanen, J., & Svensson, R. 1996, *ApJ*, 470, 249
- Reeves, J. N., et al. 2007, *PASJ*, 59, S301
- Reynolds, C. S. 1997, *MNRAS*, 286, 513
- Sambruna, R. M., Eracleous, M., & Mushotzky, R. F. 1999, *ApJ*, 526, 60
- Serlemitsos, P. J., et al. 2007, *PASJ*, 59, S9
- Takahashi, T., et al. 2007, *PASJ*, 59, S35
- Tanaka, Y., et al. 1995, *Nature*, 375, 659
- Turner, T. J., George, I. M., Nandra, K., & Turcan, D. 1999, *ApJ*, 524, 667
- Turner, T. J., Kraemer, S. B., George, I. M., Reeves, J. N., & Bottorff, M. C. 2005, *ApJ*, 618, 155
- Turner, T. J., Weaver, K. A., Mushotzky, R. F., Holt, S. S., & Madejski, G. M. 1991, *ApJ*, 381, 85
- Ueno, M., et al. 2007, *PASJ*, 59, S171
- Urry, C. M., & Padovani, P. 1995, *PASP*, 107, 803
- Vaughan, S., & Fabian, A. C., 2004, *MNRAS*, 348, 1415
- Walker, R. C., Benson, J. M., & Unwin, S. C. 1987, *ApJ*, 316, 546
- Wandel, A., Peterson, B. M., & Malkan, M. A. 1999, *ApJ*, 526, 579
- White, L. R., et al. 2000, 126, 133
- Wilms, J., Reynolds, C. S., Begelman, M. C., Reeves, J., Molendi, S., Staubert, R., & Kendziorra, E. 2001. *A&A*, 328, L27
- Woźniak, P. R., Zdziarski, A. A., Smith, D., Madejski, G.M., & Johnson, W. N. 1998, *MNRAS*, 299, 449
- Yamaguchi, H., et al. 2006, in *Proc. The X-ray Universe 2005*, vol.2, (Noordwijk, the Netherlands : ESA), 949
- Yaqoob, T., & Padmanabhan, U. 2004, *ApJ*, 604, 63
- Zdziarski, A. A., & Grandi, P. 2001, *ApJ*, 551, 186
- Zensus, J. A. 1989 in *BL Lac Objects*, ed. L. Maraschi, T. Maccacaro, & M.-H. Ulrich (Berlin: Springer), 3
- Zhang, Y. H., et al. 2002, *ApJ*, 572, 762